Supplementary Information

Tamara Annina Gerber[1], David Armond Lilien[2], Nicholas Mossor Rathmann[1], Steven Franke[3], Tun Jan Young[4], Fernando Valero-Delgado[3], Reza Ershadi[5], Reinhard Drews[5], Ole Zeising[3], Angelika Humbert[3, 6], Nicolas Stoll[3, 6], Ilka Weikusat[3], Aslak Grinsted[1], Christine Schøtt Hvidberg[1], Daniela Jansen[3], Heinrich Miller[3], Veit Helm[3], Daniel Steinhage[3], Charles O'Neill[7], John Paden[8], Siva Prasad Gogineni[7], Dorthe Dahl-Jensen[1, 2], and Olaf Eisen[3, 6]

[1]*Section for the Physics of Ice, Climate and Earth, Niels Bohr Institute, University of Copenhagen, Copenhagen, Denmark*
[2]*Centre for Earth Observation Science, University of Manitoba, Winnipeg, Canada*
[3]*Alfred Wegener Institute, Helmholtz Centre for Polar and Marine Research, Bremerhaven, Germany*
[4]*Scott Polar Research Institute, University of Cambridge, Cambridge, United Kingdom*
[5]*Department of Geosciences, Tübingen University, Tübingen, Germany*
[6]*Department of Geosciences, University of Bremen, Bremen, Germany*
[7]*Remote Sensing Centre, University of Alabama, Tuscaloosa, USA*
[8]*Centre for Remote Sensing of Ice Sheets (CReSIS), University of Kansas, Lawrence, USA*

Contents

1 Background

When water freezes under conditions prevailing on Earth's surface, H_2O molecules are arranged in layers of hexagonal rings. The plane of these rings is called the *basal plane* and the perpendicular direction is termed the *c-axis*. A consequence of the hexagonal crystal structure is that shearing along the basal plane occurs much easier than the deformation in any other direction (Duval et al., 1983), causing mechanical anisotropy.

Glacier ice consists of billions of individual crystals, and their orientation strongly affects the bulk mechanical ice properties. After the initial deposition of snow and its transformation into ice, the c-axes generally point in random directions, so the bulk property of ice is isotropic. With time and as a consequence of ice deformation through uniaxial vertical compression and ice flow, the size, shape and orientation of crystals is altered as atoms escape from one crystal lattice to another by mechanisms generally summarized as recrystallization processes (e.g. Kamb, 1959; Kamb, 1972; Azuma and Higashi, 1985; Alley, 1988): Driven by differences in the free energy between adjacent crystal lattices, larger crystals grow at the cost of smaller ones (normal grain growth), reducing the free energy of the system. Similarly, the free energy is reduced by transferring molecules from deformed high-energy grains to low-energy grains. This so-called migration recrystallization leads to the growth of grains with a preferred orientation at the cost of others. Rotation recrystallization describes the formation of new grain boundaries caused by the alignment of dislocations through bending stresses. Lastly, new grains can nucleate in areas where the crystal lattice is highly distorted and grow by consuming their neighbours. Unlike normal grain growth and rotation recrystallization, the processes of migration recrystallization and grain nucleation alter the fabric considerably and lead to bulk anisotropy of ice, with the c-axes generally pointing in the direction of predominant compression (Gow and Williamson, 1976; Azuma and Higashi, 1985).

The orientation of ice crystals is directly measured in thin sections of ice with fabric analyzers (e.g. Wilen et al., 2003; Wilson et al., 2003) and is commonly represented as a second-order orientation tensor, $\mathbf{a}^{(2)}$, describing the density distribution of c-axes orientations: its eigenvectors, $\mathbf{a}_i$, and the corresponding eigenvalues, λ_i, describe the orientation and length of the three main axes (e.g. Durand et al., 2006; Thorsteinsson et al., 1997a; Woodcock, 1977). By convention, the three eigenvalues are defined as $\lambda_1 \leq \lambda_2 \leq \lambda_3$ and $\lambda_1 + \lambda_2 + \lambda_3 = 1$.

The crystal orientation fabric (COF) is a product of the accumulated strain, so different deformation regimes in ice sheets cause characteristic fabrics. At ice domes, the predominant strain comprises vertical compression, which increases with depth. As a result, typical fabric profiles obtained from ice cores drilled near topographic domes show a transition from roughly isotropic ice ($\lambda_1 \approx \lambda_2 \approx \lambda_3$) in the top regions of the ice sheet to a vertical single maximum of increasing strength with depth ($\lambda_3 \gg \lambda_1 \approx \lambda_2$) (e.g. Thorsteinsson et al., 1997a; Azuma et al., 1999; Durand et al., 2009; Montagnat et al., 2012; Diprinzio et al., 2005). At ice divides, horizontal extension exists in addition to the vertical compression, which typically results in a girdle fabric, where $\lambda_1 \ll \lambda_2 \approx \lambda_3$ (e.g. Wang et al., 2002a; Lipenkov et al., 1989; Faria et al., 2014; Fitzpatrick et al., 2014; Montagnat et al., 2014). Close to the bed, the deformation regime is dominated by simple shear, where a single maximum fabric oriented perpendicular to the shear plane tends to develop (e.g. Cuffey et al., 2000; Herron and Langway, 1982; Gow et al., 1997; Thorsteinsson et al., 1997a). This can also be observed by ice deformation experiments (Bouchez and Duval, 1982; Journaux et al., 2019) and in a few ice cores retrieved in shear margins (Thomas et al., 2021; Samyn et al., 2008; Gerbi et al., 2021; Monz et al., 2021), where simple shear also prevails.

Ice cores provide direct and detailed information on the COF, but the logistical cost, technical challenges, particularly in fast-flowing ice and shear margins, difficulty in reconstructing the absolute orientation of the core and their limitation of being a point measurement make ice cores impractical for a spatially extensive evaluation of the fabric type. Indirect geophysical methods applied from or above the ice surface create the link between the small scale of laboratory experiments and ice–core observations to the large-scale coverage required for ice flow models and the complete understanding of ice stream dynamics.

We combine different approaches to map the horizontal fabric anisotropy: (i) travel-time difference of radar reflections from different polarizations applied on airborne RES and ground-based pRES data (see Section 2.1 and Section 2.3), (ii) beat-signature analysis of a fabric-induced modulation of the backscattered radar power in airborne and ground-based RES profiles (Section 2.2), and (iii) numerical modelling of fabric evolution (Section 3). All applied methods yield consistent results with respect to the spatial distribution of the horizontal fabric difference across and along the ice stream and are consistent with direct observations in ice cores at the ice stream centre (EGRIP core) and the southeastern shear margin (S5 shallow core) (Section 2.4).

2 Analytical methods

The propagation of radar waves is determined by the complex relative dielectric constant

$$\varepsilon^* = \varepsilon' - i\frac{\gamma}{\omega\varepsilon_0}, \tag{1}$$

where the real part, ε', is the relative dielectric permittivity, and the imaginary part corresponds to the dielectric loss factor depending on the electrical conductivity, γ, the angular frequency, ω, and the dielectric permittivity of free space, ε_0. For simplicity, primes are omitted henceforth, and all ε symbols refer to the relative dielectric permittivity, unless stated otherwise. Most englacial reflections are caused by density contrasts in the uppermost part of the ice column (Robin et al., 1969) and impurity layers (Paren and Robin, 1975), although reflections can also occur from abrupt changes in the COF (Eisen et al., 2007; Matsuoka et al., 2012). The conductivity of ice mainly depends on its impurity content and temperatures, so the imaginary part of the permittivity constant can be assumed to be isotropic for near–vertical incidence. In contrast, the bulk permittivity shows directional dependence related to the COF.

Ice crystals show uniaxial birefringence, so the real part of the dielectric permittivity tensor of a monocrystal (superscript m) can be written as

$$\boldsymbol{\varepsilon}^m = \begin{pmatrix} \varepsilon^m_\perp & 0 & 0 \\ 0 & \varepsilon^m_\perp & 0 \\ 0 & 0 & \varepsilon^m_\parallel \end{pmatrix}, \tag{2}$$

where $\varepsilon^m_\perp$ and $\varepsilon^m_\parallel$ are the relative dielectric permittivities perpendicular and parallel to the crystal c-axis. At radar frequencies, the dielectric anisotropy of a monocrystal, $\Delta\varepsilon^m = \varepsilon^m_\parallel - \varepsilon^m_\perp$, is approximately $\Delta\varepsilon^m \simeq 0.034 - 0.035$ (Matsuoka et al., 1997).

In polycrystalline ice, the permittivity (no superscript) of the bulk tensor relates to the single ice crystal as follows (e.g. Fujita et al., 2006):

$$\boldsymbol{\varepsilon} = \begin{pmatrix} \varepsilon_x & 0 & 0 \\ 0 & \varepsilon_y & 0 \\ 0 & 0 & \varepsilon_z \end{pmatrix} = \begin{pmatrix} \varepsilon^m_\perp + \Delta\varepsilon^m\lambda_x & 0 & 0 \\ 0 & \varepsilon^m_\perp + \Delta\varepsilon^m\lambda_y & 0 \\ 0 & 0 & \varepsilon^m_\perp + \Delta\varepsilon^m\lambda_z \end{pmatrix}, \tag{3}$$

where ε_x, ε_y and ε_z correspond to the directional permittivities. Here, the coordinate system represents the principal fabric axes, whose lengths are determined by the COF eigenvalues λ_x, λ_y and λ_z. The orientation of the COF in ice sheets is related to deformation through ice flow, but the ability to determine its strength and type strongly depends on its orientation relative to the radar wave polarization. To describe these relations, we introduce four coordinate systems (Fig. 1) where x' and y' are the geographic coordinates, $\tilde{x}$ and $\tilde{y}$ point parallel and perpendicular to the ice flow direction, $\hat{x}$ and $\hat{y}$ describe the polarization directions of two orthogonal radar waves, and x and y denote the fabric Eigenframe, as mentioned above. For nadir surveys, the radar waves transmitted at the surface of ice sheets travel vertically through the ice column and are polarized perpendicular to the direction of propagation. The radar wave speed is essentially determined by the bulk dielectric permittivity in the polarization direction, hence, radio-echo sounding (RES) is only sensitive toward horizontal variations of the dielectric permittivity:

$$\Delta\varepsilon = \varepsilon_y - \varepsilon_x = \Delta\varepsilon^m(\lambda_y - \lambda_x) = \Delta\varepsilon^m\Delta\lambda. \tag{4}$$

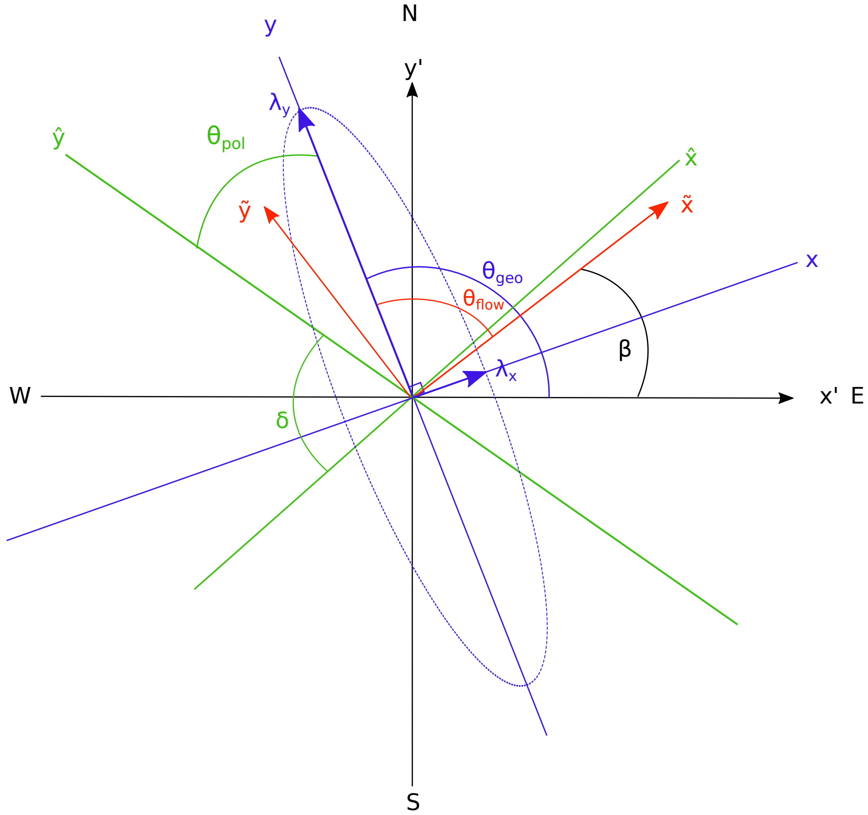

Figure 1: Coordinate systems used in this study: geographical coordinates are denoted as x' and y', equaling polar stereographic East and North respectively. Ice flows in $\tilde{x}$–direction, defined from geographic east counterclockwise by angle β. θ_{flow} is the angle between the flow direction and eigenvector corresponding larger horizontal fabric eigenvalue. The Eigenframe is denoted by x and y, whereby x points in the direction of the smaller horizontal eigenvalue. Radar waves at crosspoins are polarized in $\hat{x}$ and $\hat{y}$ respectively, and related to the Eigenframe by angle θ_{pol}. δ is the smaller angle between the polarization directions. θ_{geo} is the angle between geographic East and the larger horizontal eigenvalue.

We therefore assume the vertical direction, z, is consistent for all coordinate systems and define it as depth below the ice surface.

The electromagnetic wave speed, c, is determined by the complex dielectric constant as follows:

$$c = \frac{c_0}{\sqrt{\varepsilon *}} \approx \frac{c_0}{\sqrt{\varepsilon}}, \tag{5}$$

where c_0 is the speed of light in free space. Since the real part of the relative dielectric constant of ice is several orders of magnitude larger than the dielectric loss factor, the latter has a diminishing effect, so the wave speed primarily depends on ε. If the dielectric permittivities vary in two polarization directions, i.e. $\varepsilon_{\hat{x}} \neq \varepsilon_{\hat{y}}$, the wave speeds and wavelengths of two radar waves polarized in $\hat{x}$ and $\hat{y}$ differ slightly. Consequently, the travel time difference, Δt, between the reflected signal of radar waves with different antenna polarizations is related to the horizontal anisotropy of the ice.

As introduced in the online methods, radar waves are decomposed in ordinary and extraordinary rays when travelling through polycrystalline ice with bulk anisotropic dielectric properties. In the following section, we describe the individual methods we use for deriving horizontal anisotropy from signatures caused by radar wave decomposition.

2.1 Travel-time analysis of radar crosspoints

The EGRIP-NOR-2018 radar dataset was recorded as a dense grid across the ice stream with antennas polarized parallel to the flight direction (HH), so at each radar line crosspoint (CP), two radar traces with different antenna polarizations lie close to each other. The travel-time difference, Δt, between two orthogonally polarized waves is related to the horizontal fabric anisotropy through:

$$\Delta t = t_{\hat{y}} - t_{\hat{x}} = \frac{2(\sqrt{\varepsilon_{\hat{y}}} - \sqrt{\varepsilon_{\hat{x}}})}{c_0} z, \tag{6}$$

where $t_{\hat{x}}$ and $t_{\hat{y}}$ are the recorded two-way travel times in the corresponding polarization directions $\hat{x}$ and $\hat{y}$.

2.1.1 Travel–time picking and time-depth conversion

We manually picked $t_{\hat{x}}$ and $t_{\hat{y}}$ of prominent reflections observed in the closest traces of crossing radar profiles with intersection angles of approximately 90°. To account for eventual differences in the flight height of the aircraft, we shifted time zero to the first break of the air–ice interface. We moreover used a spline interpolation to increase the temporal resolution from 0.033 μs to 0.001 μs.

In the EastGRIP ice core, the dielectric permittivity was inferred from Dielectric Profiling (DEP) by Mojtabavi et al. (2020) and is used here to estimate the electromagnetic wave-speed profile through the ice column. In the firn layers, the dielectric permittivity is controlled by the density and increases with depth. Below the transition into pure ice, changes in the permittivity, and thus also in the electromagnetic wave speed, occur mainly due to the COF. However, the instrument sensitivity of the DEP device is not high enough to measure these effects (Wilhelms et al., 1998). To estimate the radar wave speeds while eliminating instrument noise, we assume a firn permittivity of 1.55 (Mojtabavi et al., 2022) at the ice-sheet surface and extrapolate the smoothed DEP profile (moving average with 5 m window length) from the core onset (13 m depth) to the surface. Below the transition into pure ice at ∼200 m we assume a constant permittivity of 3.15.

While the DEP-inferred wave-speed profile is a reasonable representation at EastGRIP, we recognize that variations and inhomogeneities in firn densification can lead to spatially varying wave speed profiles. While temperature and accumulation rate only vary mildly over distances relevant in this study, increased deformation accelerates densification in the shear margins (e.g. Riverman et al., 2019; Vallelonga et al., 2014; Christianson et al., 2014; Oraschewski and Grinsted, 2021). Consequently, the vertical density and electromagnetic wave speed gradients can be expected to be stronger in the vicinity of the shear margins. Assuming a spatially constant wave speed profile could therefore affect the analysis of the CPs in the immediate vicinity of the shear margins. Most

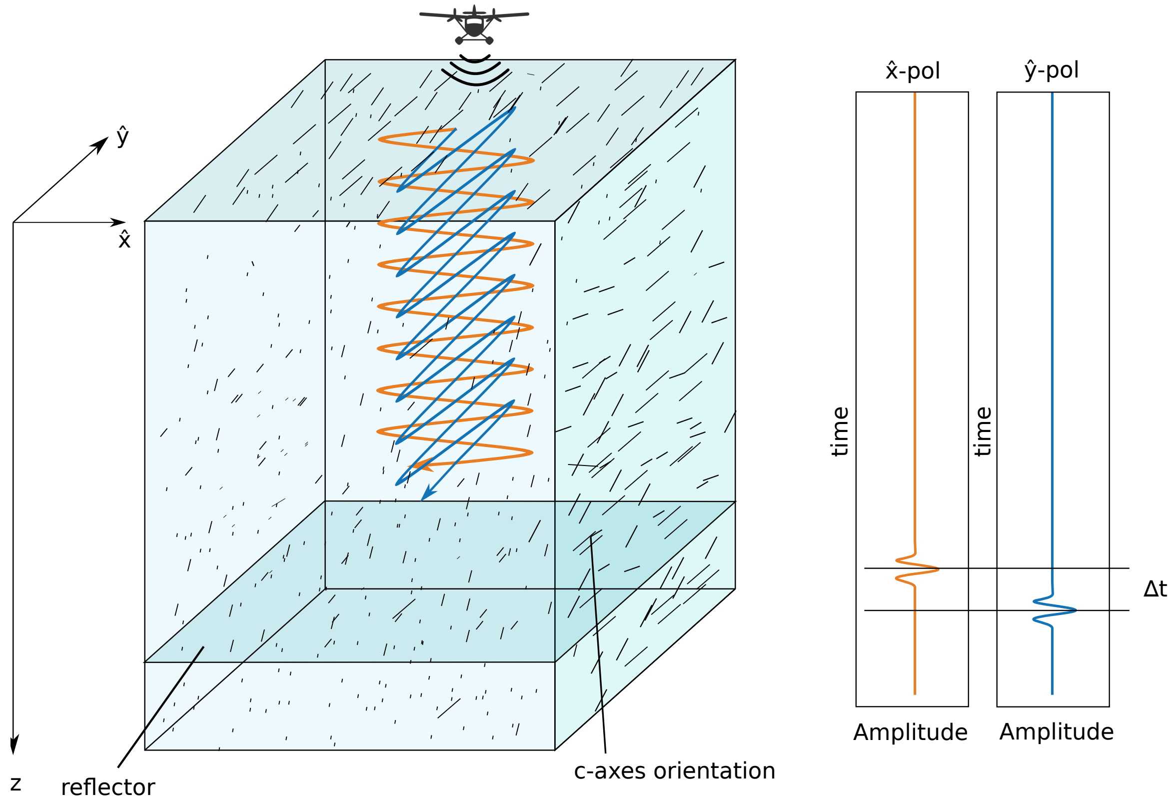

Figure 2: A reflecting interface at depth z and a horizontally anisotropic fabric leads to a travel time difference (Δt) of the reflected signal. In this example, the c-axes are predominantly oriented in x-direction, so the x-polarized wave travels at a slightly slower velocity and the reflection signal is delayed in comparison to the y-polarized signal.

of the CPs analyzed here are more than 2 km away from the shear zone, though, so the wave speed assumption is arguably justified in most cases.

The depth of the picked reflections is estimated by converting the average travel times $\bar{t} = \frac{1}{2}(t_{\hat{x}} + t_{\hat{y}})$ to depth, using the DEP-based wave-speed profile. From Eq. (6) we define a maximum threshold for the depth-dependent travel-time anisotropy resulting from a horizontal single maximum fabric, assuming that $\varepsilon_{\parallel}^{m} = 3.167$ and $\varepsilon_{\perp}^{m} = 3.133$, i.e. $\Delta\varepsilon^{m} = 0.034$ (Matsuoka et al., 1997). Picked reflections where Δt exceeds the corresponding threshold are considered outliers and discarded. We further remove picked reflections that deviate by more than two standard-deviations from the trend of the time–depth profile. Crosspoints, where less than five reflections could be clearly identified, are excluded from further analyses.

2.1.2 Deriving the apparent horizontal fabric anisotropy

The picked two-way travel times ($t_{\hat{x}}, t_{\hat{y}}$) of two waves reflected at the same depth, z, but polarized in $\hat{x}$ and $\hat{y}$ directions respectively, are given by:

$$t_{\hat{x}} = \frac{2\sqrt{\varepsilon_{\hat{x}}(z)}}{c_0} z \quad \text{and} \quad t_{\hat{y}} = \frac{2\sqrt{\varepsilon_{\hat{y}}(z)}}{c_0} z. \tag{7}$$

While inferring the depth-varying permittivities from Eq. (7) is possible in theory, it is unfeasible here due to the relatively large uncertainties on $t_{\hat{x}}$ and $t_{\hat{y}}$ (elaborated on below). By replacing $\varepsilon_{\hat{x}}$ and $\varepsilon_{\hat{y}}$ with the depth-averaged permittivities $\overline{\varepsilon_{\hat{x}}}$ and $\overline{\varepsilon_{\hat{y}}}$, Eq. (7) can be linearized so

$$t_{\hat{x}} = \frac{2\sqrt{\overline{\varepsilon_{\hat{x}}}}}{c_0} z = m_{\hat{x}} z \quad \text{and} \quad t_{\hat{y}} = \frac{2\sqrt{\overline{\varepsilon_{\hat{y}}}}}{c_0} z = m_{\hat{y}} z. \tag{8}$$

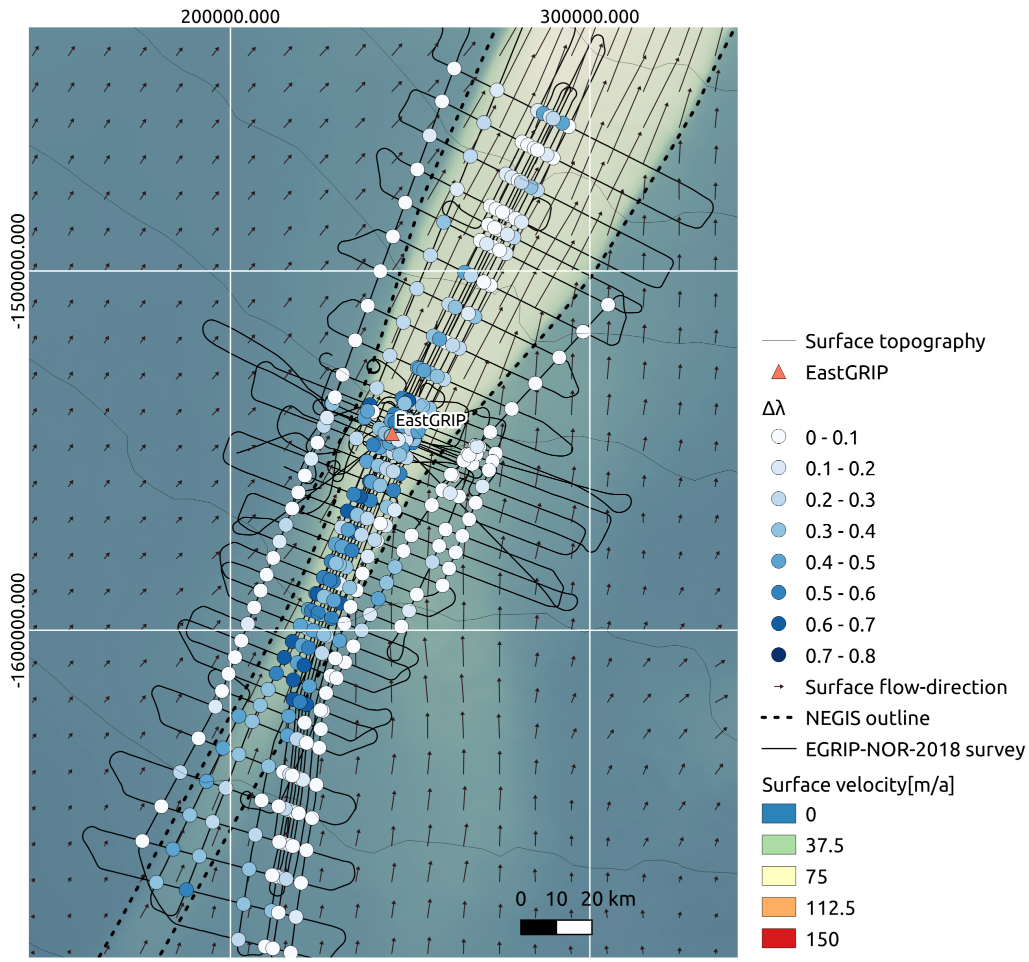

Figure 3: Horizontal fabric anisotropy ($\Delta\lambda$) from the travel-time analysis at radar crosspoints. The low anisotropy outside the shear margins is likely associated with the misalignment of radar polarization and fabric orientation.

By determining the slopes $m_{\hat{x}}$ and $m_{\hat{y}}$ from a linear regression through the picked travel times, the depth-averaged apparent horizontal dielectric anisotropy ($\Delta\varepsilon_a$) can be derived from

$$\Delta\varepsilon_a = \overline{\varepsilon_{\hat{x}}} - \overline{\varepsilon_{\hat{y}}} = \frac{c_0^2}{4}(m_{\hat{x}}^2 - m_{\hat{y}}^2), \tag{9}$$

which relates to the apparent difference in the horizontal eigenvalues as follows:

$$\Delta\lambda_a = \lambda_{\hat{x}} - \lambda_{\hat{y}} = \frac{\Delta\varepsilon_a}{\Delta\varepsilon^m}. \tag{10}$$

We emphasize that the apparent horizontal anisotropy ($\Delta\lambda_a$) inferred by this method is not equivalent to the absolute horizontal fabric anisotropy ($\Delta\lambda$) if the polarization of the two radar traces does not align with the two horizontal eigenvectors. $\Delta\lambda_a$ can thus be regarded as a lower-bound estimate of the horizontal anisotropy. Figure 3 shows the horizontal anisotropy for all analyzed crosspoints. The map of horizontal anisotropy of all analyzed crosspoints (Fig. 3) shows that almost no evidence of anisotropy is obtained for CPs outside of the shear margins. This disagrees with the results obtained from other methods (i.e. beat-signature analysis and Elmer/Ice fabric evolution model) and is likely a consequence of the method sensitivity towards the alignment between radar polarization and fabric orientation. In comparison to the other methods used in this study, the crosspoint analysis of travel-time anisotropy is regarded to be less reliable outside the ice stream.

To evaluate the robustness of our method, we compare six CPs close to the EastGRIP drill site that are separated by less than 50 m from each other. Within this distance, fabric variations can be assumed to be negligible. We investigate the sensitivity to varying depths by employing three linear regressions through different depth points at 0 m, 200 m and 500 m. The corresponding travel times at 200 m and 500 m are calculated from the $\overline{\varepsilon_{\hat{x}}}$ and $\overline{\varepsilon_{\hat{y}}}$ inferred from the regression through the origin. The regressions running through 200 m and 500 m result in higher horizontal anisotropy values due to the higher relative weight of greater depths, where the fabric is likely to be more pronounced (Table 2). Table 1 shows an example of the analysis for CP3.

Table 1: Example of travel-time anisotropy analysis for CP 3: $t_{\hat{x}}$ and $t_{\hat{y}}$ are the travel times picked from reflections at depth z from $\hat{x}$- and $\hat{y}$-polarized radar traces, respectively. Δt is the travel-time anisotropy ($t_{\hat{y}} - t_{\hat{x}}$). Superscript 0 indicates travel times and travel-time anisotropy from a linear regression through the origin, superscript 200 m and 500 m denote the corresponding values for linear regression through 200 m and 500 m points (in italic) respectively. $\overline{\varepsilon_{\hat{x}}}$, $\overline{\varepsilon_{\hat{y}}}$ and $\Delta\varepsilon_a$ at the bottom of the table are the directional dielectric permittivities and apparent horizontal permittivity anisotropy derived from the corresponding linear regression.

z	$t_{\hat{x}}$	$t_{\hat{y}}$	Δt	$t^0_{\hat{x}}$	$t^0_{\hat{y}}$	Δt^0	$t^{200}_{\hat{x}}$	$t^{200}_{\hat{y}}$	Δt^{200}	$t^{500}_{\hat{x}}$	$t^{500}_{\hat{y}}$	Δt^{500}
0	-	-	-	*0*	*0*	*0*	-	-	-	-	-	-
200	-	-	-	-	-	-	*2.347*	*2.353*	*0.0063*	-	-	-
459.8	5.313	5.319	0.005	5.395	5.409	0.015	5.397	5.412	0.015	-	-	-
484.6	5.604	5.614	0.009	5.686	5.701	0.015	5.688	5.704	0.016	-	-	-
500	-	-	-	-	-	-	-	-	-	*5.866*	*5.882*	*0.016*
540.9	6.269	6.283	0.013	6.346	6.363	0.017	6.349	6.367	0.018	6.357	6.376	0.019
560	6.504	6.500	-0.004	6.570	6.588	0.018	6.573	6.591	0.018	6.582	6.602	0.020
709.3	8.272	8.267	-0.005	8.322	8.344	0.022	8.326	8.349	0.023	8.336	8.362	0.025
735.7	8.580	8.586	0.006	8.632	8.655	0.023	8.635	8.659	0.024	8.646	8.673	0.026
755.8	8.813	8.828	0.016	8.868	8.891	0.024	8.871	8.896	0.025	8.883	8.910	0.027
772.6	9.014	9.025	0.011	9.065	9.089	0.024	9.068	9.094	0.025	9.080	9.108	0.028
782.1	9.133	9.132	-0.001	9.176	9.201	0.025	9.180	9.206	0.026	9.192	9.220	0.028
807.5	9.425	9.441	0.016	9.474	9.500	0.026	9.478	9.505	0.026	9.490	9.519	0.029
828.3	9.674	9.683	0.009	9.718	9.744	0.026	9.722	9.749	0.027	9.735	9.764	0.030
851.9	9.949	9.968	0.019	9.995	10.022	0.027	9.999	10.027	0.028	10.012	10.043	0.030
931.7	10.889	10.917	0.028	10.931	10.961	0.030	10.936	10.966	0.030	10.950	10.983	0.033
981.8	11.481	11.511	0.030	11.519	11.550	0.031	11.524	11.556	0.032	11.539	11.574	0.035
1030.4	12.064	12.080	0.016	12.089	12.122	0.033	12.094	12.128	0.034	12.110	12.147	0.037
1165.2	13.648	13.688	0.039	13.671	13.708	0.037	13.677	13.715	0.038	13.694	13.736	0.042
1222.5	14.324	14.369	0.045	14.343	14.382	0.039	14.349	14.389	0.040	14.368	14.411	0.044
1916.8	22.525	22.608	0.082	22.489	22.550	0.061	22.499	22.561	0.063	22.528	22.596	0.069
2048.5	24.085	24.167	0.082	24.034	24.099	0.065	24.045	24.111	0.067	24.075	24.149	0.073
2166.1	25.475	25.562	0.087	25.414	25.483	0.069	25.425	25.496	0.071	25.458	25.535	0.077
2674.3	31.491	31.580	0.089	31.377	31.461	0.085	31.390	31.477	0.087	31.430	31.526	0.096
				$\overline{\varepsilon_{\hat{x}}}$	$\overline{\varepsilon_{\hat{y}}}$	$\Delta\varepsilon_a$	$\overline{\varepsilon_{\hat{x}}}$	$\overline{\varepsilon_{\hat{y}}}$	$\Delta\varepsilon_a$	$\overline{\varepsilon_{\hat{x}}}$	$\overline{\varepsilon_{\hat{y}}}$	$\Delta\varepsilon_a$
				3.093	3.110	0.017	3.096	3.113	0.017	3.104	3.122	0.019

Uncertainties in travel-time anisotropy

Most uncertainties in this method arise from determining the travel times $t_{\hat{x}}$ and $t_{\hat{y}}$. The range resolution of the recorded signal corresponds to a temporal resolution of 0.033 μs, but by interpolating the waveform within the sampling interval, we reduce the picking uncertainty to roughly $\pm$ 0.01 μs. The compared radar traces were not recorded concurrently in space and time, so differences

Table 2: Comparison of travel-time analysis at six crosspoins near EastGRIP (Fig. 4). The table shows the apparent horizontal anisotropy $\Delta\lambda_a$ inferred from a regression through the origin, $\Delta\lambda_a^0$, 200 m, $\Delta\lambda_a^{200}$, and 500 m, $\Delta\lambda_a^{500}$. δ is the angle between the two crossing flight lines and $\tilde{a}(\Delta\lambda_a)$ and $\tilde{s}(\Delta\lambda_a)$ are the mean and standard deviations of $\Delta\lambda$ inferred from the three different regression lines.

CP	$\Delta\lambda_a^0$	$\Delta\lambda_a^{200}$	$\Delta\lambda_a^{500}$	δ
1	0.435	0.448	0.488	89.9
2	0.389	0.403	0.443	78.0
3	0.492	0.508	0.556	86.1
4	0.400	0.405	0.433	86.6
5	0.505	0.515	0.546	89.7
6	0.381	0.400	0.456	89.2
$\tilde{a}(\Delta\lambda)$	0.434	0.447	0.487	
$\tilde{s}(\Delta\lambda)$	0.054	0.053	0.053	

in background noise can arise from variations in weather conditions, flight height or surface structures and might lead to signal alteration. The distance between the parallel-flow and the across-flow radar traces is 11.7 m at maximum, so geometrical effects are assumed to be small but cannot be excluded entirely. Further uncertainties could be introduced from the time–to–depth conversion and the assumption of a spatially constant electromagnetic wave speed profile.

2.2 Beat-signature analysis

For a transmitted wave whose polarization plane is not aligned with one of the horizontal anisotropy axes, the electric field can be regarded as the superposition of two components, E_x and E_y. The difference in the wave speed leads to a phase shift and hence a polarization rotation, causing extinction nodes in radar return power (Matsuoka et al., 2012; Fujita et al., 2006). In the absence of anisotropic scattering, these nodes are most pronounced when the transmitted wave is polarized at an angle of 45° from the horizontal eigenvector $\mathbf{a}_x$, and the phase differences are proportional to the radar wave frequency and the degree of horizontal anisotropy (Fujita et al., 2006). As explained above, the difference in the horizontal components of the bulk dielectric permittivities $\Delta\varepsilon$ defined in Eq. (4) causes a continuous difference in two-way travel time, $\Delta t(z)$, of the two principle waves, which can also be expressed as a phase difference $\phi(z) = 2\omega\Delta t(z)$, where the factor 2 arises from the consideration of two-way traveling and $\omega = 2\pi f$ is the angular frequency of the radar wave with center frequency f. The change of ϕ with depth gives rise to a continuous modulation of the backscattered power. In analogy to signal mixing, this can also be considered as a beat or modulation frequency f_{mod} from two superimposed waves at slightly different frequencies or wavelengths, in our cases originating from the wave speed differences, as expressed in (6). The beat-signature results in destructive interference, a so-called co-polarization extinction node, when the phase difference ϕ between the ordinary and extraordinary wave is an odd multiple of π (Fujita et al., 2006). Neglecting anisotropic backscatter and approximating Eq. (13) in Fujita et al. (2006) with a Taylor expansion (Jordan et al., 2019) results in

$$\phi(z) = \frac{4\pi f}{c_0}\int_z^0 \frac{\Delta\varepsilon(z)}{2\sqrt{\varepsilon_{xy}}}dz = \frac{2\pi f}{c_0}\Delta\varepsilon^m \int_z^0 \frac{\Delta\lambda(z)}{\sqrt{\varepsilon_{xy}}}dz \tag{11}$$

where ε_{xy} is the mean of the horizontal relative permittivities. Assuming a vertically constant fabric with a constant difference $\Delta\lambda$ and thus permittivities, equation (11) simplifies to

$$\phi(z) = \frac{2\pi f \Delta\varepsilon^m}{c_0\sqrt{\varepsilon_{xy}}}\Delta\lambda z. \tag{12}$$

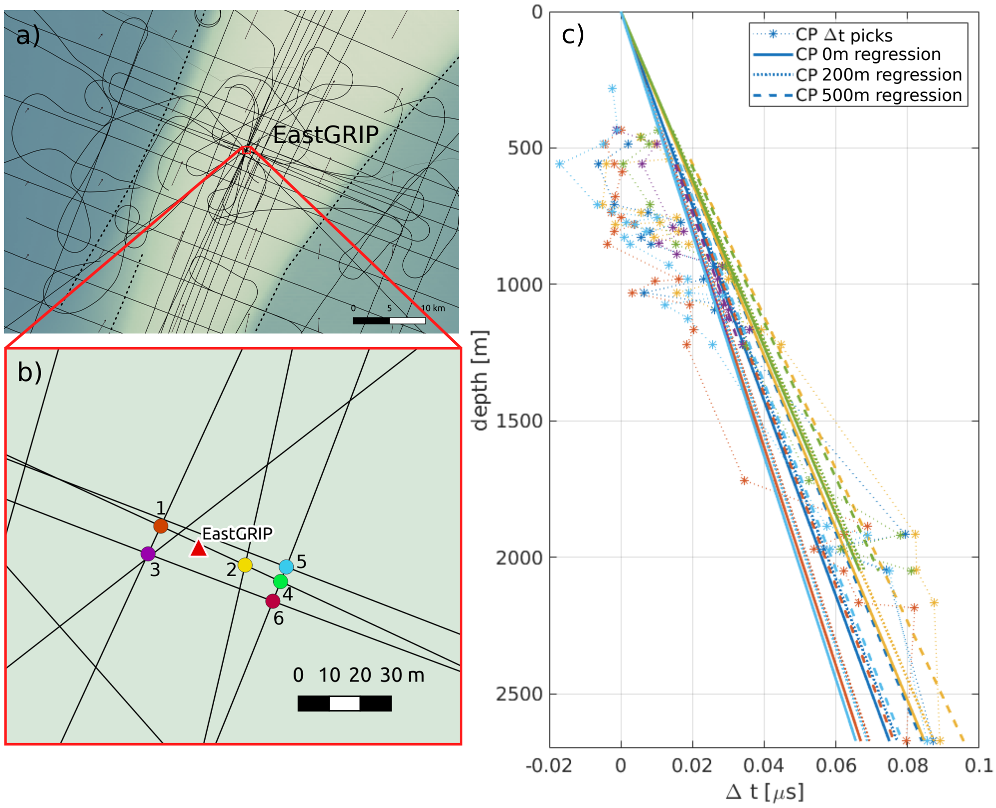

Figure 4: **a), b**) Location and **c)** travel-time difference of six crosspoints in the vicinity of EastGRIP. The right panel shows difference in the picked travel times with depth (dashed lines) and the fit of a first-degree polynomial (solid line) from which the apparent horizontal anisotropy $\Delta\lambda_a$ was derived.

Using the wave number k_{mod} of the beat signature to relate the phase difference ϕ to propagated depth z allows us to write

$$\phi(z) = 2k_{mod}z = \frac{4\pi\sqrt{\varepsilon_{xy}}f_{mod}}{c_0}z. \tag{13}$$

Here, again, the first factor of 2 arises from the consideration of two-way propagation.

Setting equation (13) equal to (12) finally yields

$$\Delta\lambda = \frac{2\varepsilon_{xy}}{\Delta\varepsilon^m}\frac{f_{mod}}{f}, \tag{14}$$

thus linearly connecting the horizontal anisotropy to the beat frequency f_{mod} and the center frequency f of the radar system.

In Eq. (14), we can also use the period $T_{mod} = f_{mod}^{-1}$ of the beat signal, e.g. directly from a radargram in the time domain and pick the time difference between neighboring minima/nodes, to obtain

$$\Delta\lambda = \frac{2\varepsilon_{xy}}{f\Delta\varepsilon^m}\frac{1}{T_{mod}}. \tag{15}$$

Minima in the beat signal are caused if the two waves are out of phase, i.e. if they have a phase difference of uneven multiples of π, $\Delta\phi = (2n+1)\pi$. Considering the beat signal as the image of a wave in the two-way travel-time domain (as we can see it in the radargram) with phase θ_{mod} we can write

$$\theta_{mod} = k_{mod}s = k_{mod}\frac{c_0 t}{\sqrt{\varepsilon}}, \tag{16}$$

with $k_{mod} = \frac{2\pi}{l_{mod}}$ being the wave number and l_{mod} the wavelength of the beat (or modulation) signal. The second factor s is the propagated path, which can be calculated from the two-way travel time t.

The travelpath s is twice the actual depth as plotted in a radargram, $s = 2z$, and therefore

$$\theta_{mod} = 2k_{mod}z. \tag{17}$$

In the simplest case of two neighboring minima, separated by depth Δz, the phases θ_{mod} at these two minima are 2π apart, i.e. $\Delta\theta_{mod} = 2\pi$. Thus we can write

$$\Delta\theta_{mod} = 2\pi = 2k_{mod}\Delta z = 2\frac{2\pi}{l_{mod}}\Delta z \tag{18}$$

which is yields

$$l_{mod} = 2\Delta z. \tag{19}$$

i.e. the wavelength l_{mod} of the beat signal is twice the distance between two minima.

Young et al. (2021) exploited this effect along shallow airborne radar profiles over the eastern shear margin of Thwaites Glacier to deduce the bulk anisotropy in the upper part of the ice sheet. We apply the same approach here to derive the vertical fabric variations, as described in the following subsections.

2.2.1 Manual determination of horizontal anisotropy from birefringence-induced power loss

To investigate the possibility of depth-variable fabric asymmetry (or to evaluate the limitations of the assumption of a depth-constant fabric asymmetry), we employ the semi-manual methods of Young et al. (2021) over a representative subset of radargrams aligning both parallel and perpendicular to the ice-flow direction. For each radargram frame, the birefringent minima are manually traced following a two-dimensional convolution with window dimensions of 138×344 m^2 and 87×278 m^2 for the UHF 750 MHz and AWI-UWB 195 MHz radargrams, respectively. The resulting traces are then automatically aligned to and smoothed over the 'true' locations of the nearest birefringent minima using a Gaussian-weighted moving average algorithm with a 500 m window. Examples for two profiles perpendicular to ice flow and near the EastGRIP drill site are shown in Fig. 5 (UHF system with 750 MHz) and Fig. 6 (AWI-UWB system with 195 MHz). The method, in principle, also allows to determine the variation of the fabric with depth, averaging over the vertical distance of two nodelines.

2.2.2 Semi-automatic determination of horizontal anisotropy from beat frequency

Although the manual determination of the fabric resolves vertical variations of the beat frequencies – i.e. the distance between node lines – to derive the variation of the horizontal fabric difference, the applicability to large data sets is limited as it is a very time-consuming process. We therefore developed an automated approach, which extracts the beat frequency f_{mod} from radargrams by spectrogram analysis. The AWI UWB radargrams, which have been processed in the standard processing chain (see Franke et al., 2022), are further processed by a bandpass filter (100–750 kHz), time cutting the upper section to remove the surface multiple and the lower section with the bed reflection and strong folds, and a second application of the same bandpass filter. The remaining part of the radargram contains backscatter variations mainly caused by internal layers, most of which are of volcanic origin (Mojtabavi et al., 2022) and the beat-frequency modulation of the backscattered power caused by horizontal anisotropy. All pre-processed traces of a radargram are then concatenated to obtain one long time series. We use the MATLAB^{TM} *spectrum* function to calculate a continuous spectrum of the time series, using frequency limits of 100 to 750 kHz, default segmentation with 50% overlap of neighbouring segments for spectral estimates. This results in a spectrogram of the radar return power in the range of 100–750 kHz along the radar profile. Depending on the location, the spectrograms clearly show modes originating from the beat frequency (Fig. 7). In a next step, we automatically extract the frequency of those dominating modes as a function of position, which is then manually checked for consistency and corrected for artefacts. Finally, we obtain a distribution of the dominating beat frequency, which is converted to $\Delta\lambda$ by Eq. (14) (see Fig. 7 for an example). The approach is very efficient, as the radargrams can be processed automatically. We estimate the

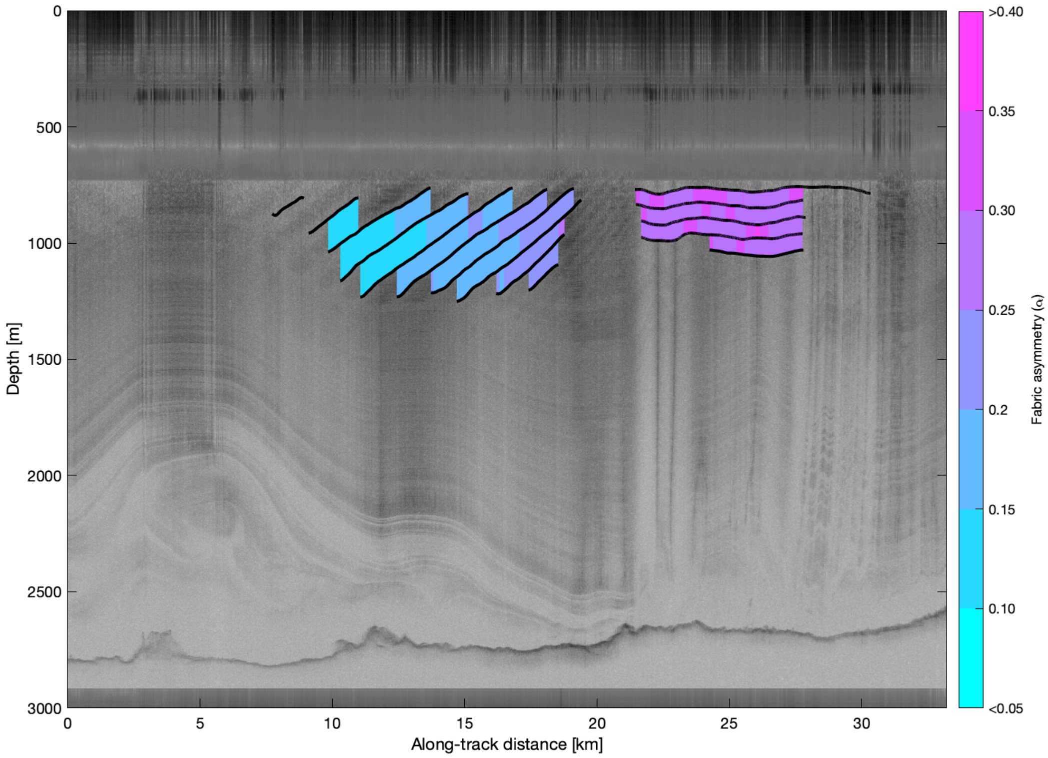

Figure 5: Radargram recorded with the UHF Mills Cross system (Yan et al., 2020) with a center frequency of 750 MHz. The profile runs from EastGRIP (right) towards the north, perpendicular to ice flow and across the shear margin, with a turn at the end (left). The signature in the upper 700 m shows an artifact from the source chirp, the bed reflection is visible around 2700–2800 m. Between 700 and 1200 m depth, beat signatures are highlighted. The horizontal fabric anisotropy is derived from the distance of neighboring node lines and is indicated by color, using the approach of Young et al. (2021) . Lower panels indicate surface z_s (black) and bed z_b (red) elevation along radargram transect from BedMachine and surface velocity u_s (black) and lateral shear strain τ_{xy} (red) along radar transect derived from ITS LIVE surface velocities (Gardner et al., 2021).

uncertainty in $\Delta\lambda$ to be around 0.05, i.e. 5% of its theoretical maximum. However, the limitations are in parts ambiguities in the spectral analysis, for instance, if internal layers are spaced at an equal vertical distance comparable to the beat signatures. The approach is, therefore, most applicable in regions where the horizontal anisotropy is spatially changing, i.e. along radar profiles perpendicular to the flow field and across the shear margins. The results are best suited for the interpretation of the overall spatial distribution of the anisotropy rather than depicting the fabric at a particular location without taking the spatial distribution into account.

2.2.3 Forward modelling of birefringence induced anisotropy

To demonstrate the effect of modelled polarimetric radio signal propagation through an ice column, we use the Fujita et al. (2006) matrix-based model for a frequency of $f = 195$ MHz. Each model case in Fig. 8 shows the effect of a slightly different horizontal anisotropy within the ice column defined by increasing the difference between the two horizontal eigenvalues ($\Delta\lambda$). The other parameters in the models, including the anisotropic scattering (set to zero) and fabric orientation, remain constant. More details about the features in the forward model and the effect of other parameters are explained in Ershadi et al. (2022).

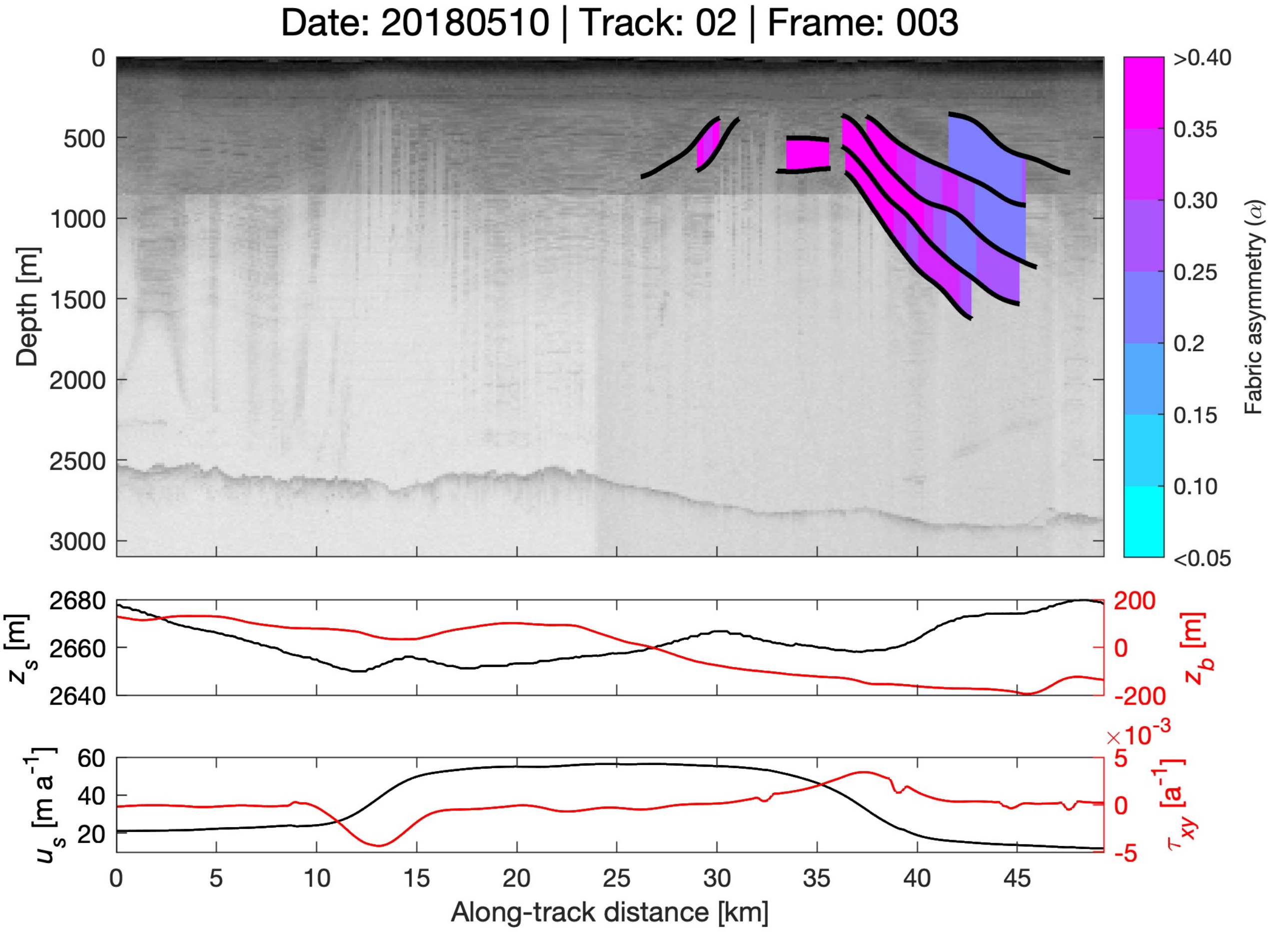

Figure 6: Radargram recorded with the AWI UWB radar system with a center frequency of 195 MHz. The profile crosses NEGIS, with EastGRIP in the center, from southeast (left) to northwest (right), perpendicular to ice flow and across both shear margins. The part northwest of EastGRIP is close to the ground-based radar profile shown in Figure 5. The horizontal fabric anisotropy derived from the distance of neighboring node lines is again indicated by color, using the approach of Young et al. (2021).

2.3 Travel-time analysis of polarimetric pRES measurements

In general, the analysis of the horizontal fabric anisotropy from the polarimetric pRES measurements follows the method described in section 2.1. First, we calculate the vertical travel-time difference between the HH- and the VV-polarized measurements from the cross-correlation of the amplitude- and the phase-profiles. This method is widely used to derive vertical strain from repeated pRES measurements (e.g. Stewart et al., 2019; Vaňková et al., 2020; Zeising and Humbert, 2021) and is described in detail in Stewart (2018). Before calculating the cross-correlation, we apply the time-depth conversion and divide the HH-polarized measurement into segments of 6 m depth with 3 m overlaps, starting at a depth of 20 m. The cross-correlation between the HH- and the VV-polarized measurements are then calculated for each segment. A first coarse range difference with a resolution of $>$ 5 cm is derived from the lag with the largest amplitude-correlation value for segments with a correlation coefficient higher than 0.8. However, a low signal-to-noise level prevents the estimation of the coarse-range difference from a depth of roughly 1500 m and deeper.

In order to derive the fine-range difference with millimeter-resolution, we use the phase shifts from the cross-correlation of the phase profiles. Here, we manually track the vertical distribution of the minimum phase-shift nearby the coarse-range differences. We finally derive the vertical distribution of the range difference (Δz) and the corresponding travel-time anisotropy (Δt) from the selected lag and phase shift of each segment.

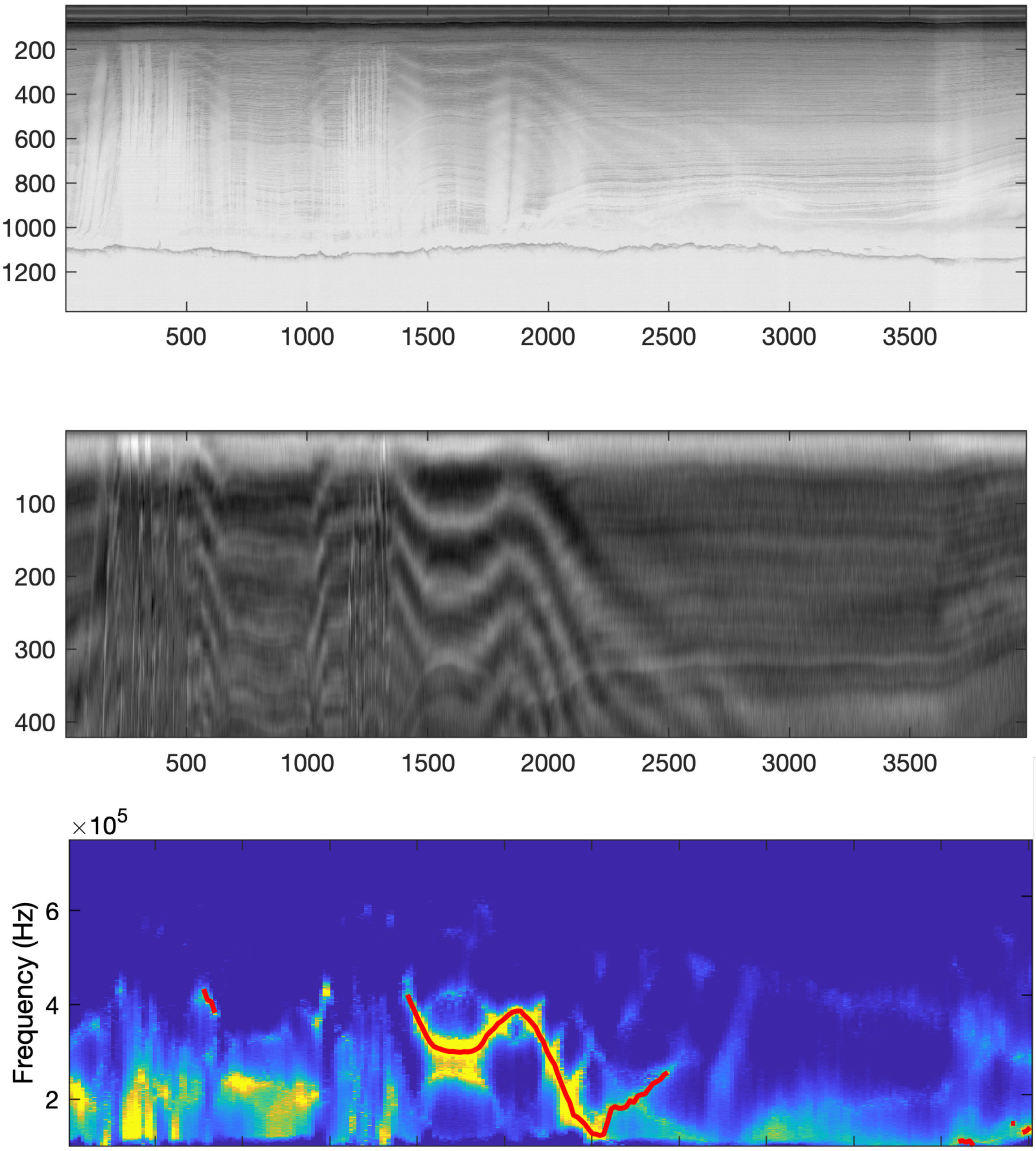

Figure 7: Example of spectrogram analysis for UWB profile 20180512-02-006 (x-axis: trace no., y-axis: sample no.): in the original radargram (top) filtered and cropped (middle), before applying the spectral analysis. From the spectrogram (bottom, relative power spectral density in colour) we obtain a manually checked and corrected distribution of f_{mod} (red line) from which the horizontal anisotropy is calculated using Eq. (14).

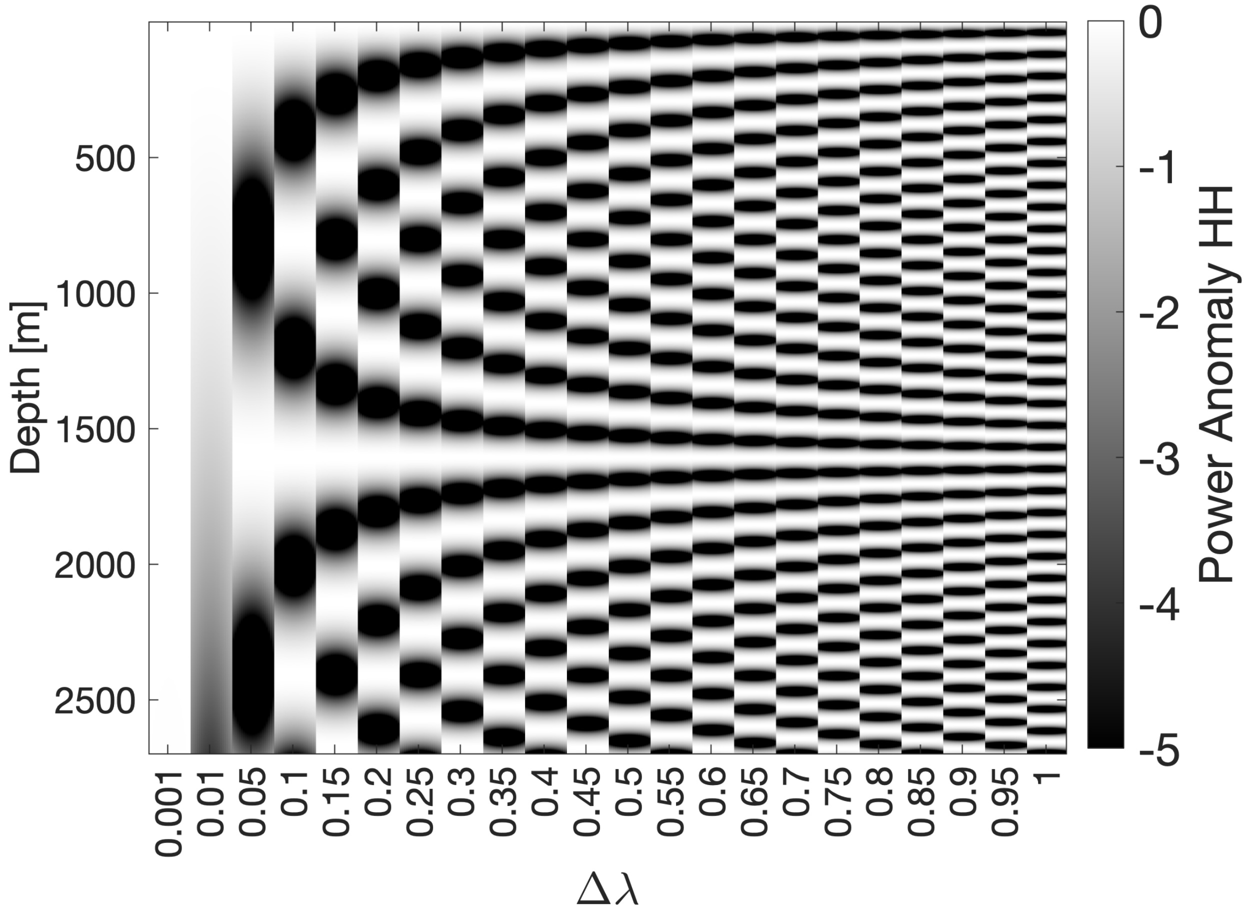

Figure 8: Synthetic calculation of power anomaly for HH polarization in a horizontally anisotropic medium for $\Delta\lambda$ ranging from 0.001 to 1 (x-axis) for an ice thickness of 2700 m (y-axis). Each of the 22 columns shows the power anomaly for a rotation of the polarization from 81 to 100°. The extinction nodes caused by birefrigence corresponds to the black nodes (i.e. lower power). Connecting nodes for a fixed polarization would yield the extinction node lines as see in radargrams (e.g. Figs. 7, 6 and 5). For very low $\Delta\lambda = 0.001$, no node is present. For $\Delta\lambda = 0.01$, the first node extends over the full ice column, for $\Delta\lambda = 0.05$ two nodes appear, etc. The calculations were done with a matrix-based model (Fujita et al., 2006; Jordan et al., 2019), closely following the approach by Ershadi et al. (2022).

Next, we calculate the horizontal fabric anisotropy from the two-way travel-time difference. In contrast to the crosspoint analysis of the airborne radar survey, the high vertical resolution of Δt obtained from pRES allows the estimation of the depth-varying permittivity. Thus, we determine the slopes $m_{\hat{x}}(z)$ and $m_{\hat{y}}(z)$ (see Eq. (8)) as a function of depth by calculating the average slopes of the travel-time difference in a 200 m moving window, after smoothing with a 24 m moving median. Finally, we derive the difference in horizontal dielectric anisotropy and the difference in the horizontal eigenvalues from Eqs. (9) and (10). An example from the measuring site 31 km upstream of EastGRIP is shown in Fig. 9.

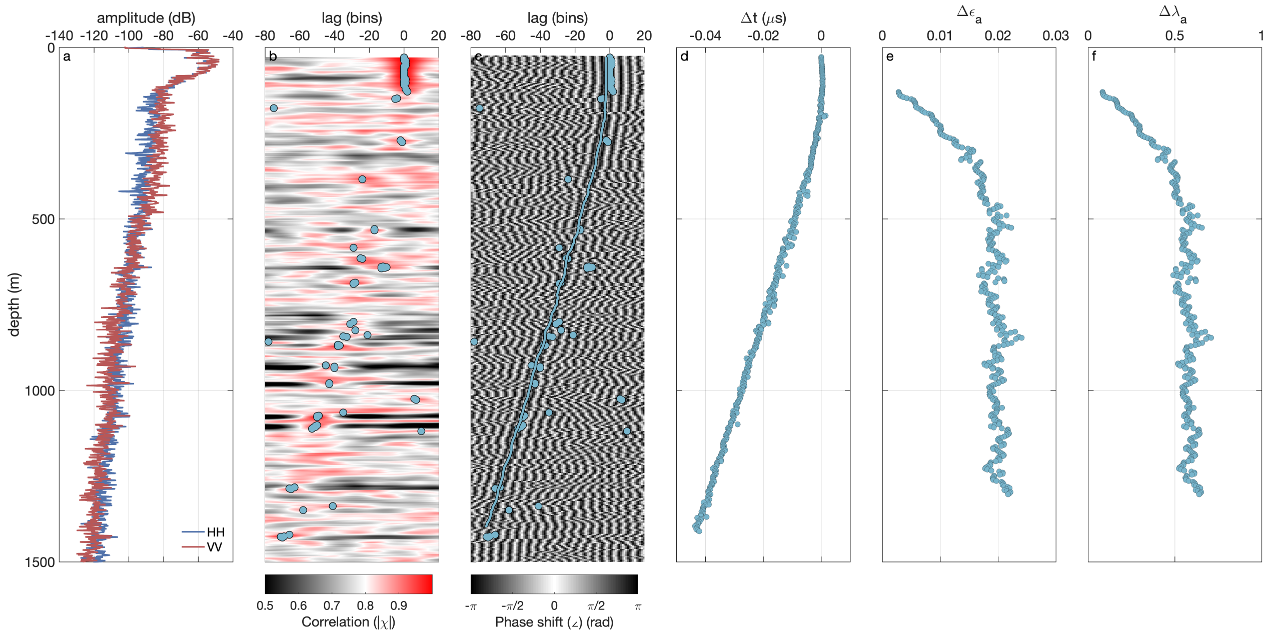

Figure 9: Analysis of the difference in horizontal eigenvalues from HH- and VV-polarised pRES measurements. The pRES measurements showed here were performed in the ice stream center, 31 km upstream of EGRIP. (a) Comparison of amplitude profiles of HH- (blue line) and VV-polarised (red line) measurement as a function of depth. (b) Cross-correlation ($|\chi|$) of both measurements as a function of lag and depth. Blue dots mark the lag of best correlation of the segment for those exceeding the correlation value of 0.8. (c) Phase shift as a function of lag and depth. The blue dots are the same as in (b). The blue line marks the tracked minimum phase shift. (d) Difference in two-way travel time between both measurements at the same depth. (e) Difference in horizontal dielectric anisotropy $\Delta\varepsilon_a$. (f) Difference in horizontal eigenvalues $\Delta\lambda_a$.

2.4 Ice core analysis

Observational fabric data was retrieved from two ice cores: the deep EastGRIP ice core and a close-by shallow core in the southeastern shear margin of NEGIS called S5. The preparation and measurement of the samples follow the same principles. All analyzed samples are vertical to the ice-core axis and have dimensions of about $90 \times 70 \times 0.3$ mm^3. The sample surfaces were carefully polished with a microtome knife in the EastGRIP trench at –18 °C. After one hour of controlled sublimation, c-axes were measured with an automated fabric analyzer by Russel-Head Instruments (FA G50). The data was background corrected before processing, and the COF was derived via digital image processing. Here, we use the COF observations to validate our observations and modeling results. The COF information from the EastGRIP ice core stems from depths of 1830 m, 2024 m, and 2087 m, as shown in Westhoff et al. (2021), and shows a vertical girdle with a superimposed horizontal single maximum. Three samples at a depth of 68 m in the S5 shallow core show a strong horizontal single maximum fabric.

3 Fabric-evolution models

We used two fabric evolution models to produce a more spatially complete map of fabric that can be compared to measurements.

3.1 Elmer/Ice

Elmer/Ice is an open source, full-Stokes ice-flow model using the finite element method. It solves the combined problems of ice flow, heat flow and fabric evolution, thus accounting for both, the fabric evolution due to temperature and deformation as well as the effect of the fabric on the mechanical properties of ice.

3.1.1 Model equations

Ice flow is described by the incompressible Stokes equations.

$$\nabla \cdot \boldsymbol{u} = 0, \tag{20}$$

where $\boldsymbol{u}$ is the velocity, and

$$\nabla \cdot \boldsymbol{\sigma} + \rho_{\mathrm{i}}\boldsymbol{g} = 0, \tag{21}$$

where $\boldsymbol{\sigma}$ is the Cauchy stress tensor, ρ_{i} the density of ice, and $\boldsymbol{g}$ the force of gravity. These equations are linked using a nonlinear extension to the General Orthotropic Linear Flow Law (Gillet-Chaulet et al., 2005) that, by analogy to Glen's flow law, introduces nonlinearity through the second invariant of the deviatoric stress tensor (Ma et al., 2010):

$$\boldsymbol{\tau} = \eta_0 \sum_{r=1}^{3} \eta_r \mathrm{tr}(\boldsymbol{M}_r \cdot \dot{\boldsymbol{\epsilon}})\mathrm{dev}(\boldsymbol{M}_r) + \eta_{r+3}\mathrm{dev}(\dot{\boldsymbol{\epsilon}} \cdot \boldsymbol{M}_r + \boldsymbol{M}_r \cdot \dot{\boldsymbol{\epsilon}}) \tag{22}$$

where $\eta_{1\ldots6}(\boldsymbol{a}^{(2)})$ are six dimensionless viscosities as a function of the fabric, tr denotes trace, dev the deviatoric portion of a tensor, $\boldsymbol{M}_{1\ldots3}$ the structure tensors that are the dyadic products of the fabric's symmetry axes (i.e. of the eigenvectors of $\boldsymbol{a}^{(2)}$), and $\eta_0 = (\tau_e^{1-n})/2A(T)$, with τ_e the second invariant of $\mathrm{dev}(\boldsymbol{\sigma})$. $A(T)$ is the temperature-dependent prefactor from Glen's flow law, and n the flow-law exponent (taken to be 3). The $\eta_{1\ldots6}(\boldsymbol{a}^{(2)})$ were found using a visco-plastic self-consistent model (Castelnau et al., 1998), assuming that ice with a single maximum fabric deforms 10 times more quickly than isotropic ice given equal shear stress while it compresses 2.5 times more slowly along the direction of the fabric maximum.

The model is solved along flowtubes, so Eqs. (20) and (21) are modified to account for a parameterized, flow-transverse coordinate $\tilde{y}$. In a coordinate system with $\tilde{x}$ along flow and z vertical,

$$\frac{\partial \sigma_{\tilde{x}\tilde{x}}}{\partial \tilde{x}} + \frac{\partial \sigma_{\tilde{x}z}}{\partial z} + \frac{\sigma_{\tilde{x}\tilde{x}} - \sigma_{\tilde{y}\tilde{y}}}{W(\tilde{x})}\frac{\partial W(\tilde{x})}{\partial \tilde{x}} = 0 \tag{23}$$

and

$$\frac{\partial \sigma_{\tilde{x}z}}{\partial \tilde{x}} + \frac{\partial \sigma_{zz}}{\partial z} + \frac{\sigma_{\tilde{x}z}}{W(\tilde{x})}\frac{\partial W(\tilde{x})}{\partial \tilde{x}} = \rho_{\mathrm{i}} g \tag{24}$$

for a flowband with width $W(\tilde{x})$ (e.g. Hvidberg, 1996).

Fabric evolution was assumed to occur solely by lattice rotation so that

$$\frac{\mathrm{D}\boldsymbol{a}^{(2)}}{\mathrm{D}t} = \boldsymbol{W} \cdot \boldsymbol{a}^{(2)} - \boldsymbol{a}^{(2)} \cdot \boldsymbol{W} - (\boldsymbol{C} \cdot \boldsymbol{a}^{(2)} + \boldsymbol{a}^{(2)} \cdot \boldsymbol{C}) + 2\boldsymbol{a}^{(4)} : \boldsymbol{C} + \boldsymbol{D} \tag{25}$$

where $\boldsymbol{W}$ is the spin tensor (anti-symmetric portion of the deformation), : is the double inner product, and

$$\boldsymbol{C} = (1-\alpha)\dot{\boldsymbol{\epsilon}} + \alpha k_s A \tau_e^{n-1} \boldsymbol{\tau} \tag{26}$$

where α is an interaction parameter controlling the relative importance of bulk stress and strain in causing fabric evolution and $\boldsymbol{D}$ is used for regularization. We take $\alpha = 0.06$ (Ma et al., 2010). The term $2\boldsymbol{a}^{(4)} : \boldsymbol{C}$ in (25) is approximated using an invariant-based fit to a parameterized ODF to get $\boldsymbol{a}^{(4)}$ as a function of $\boldsymbol{a}^{(2)}$ (Gagliardini and Meyssonnier, 1999; Gillet-Chaulet et al., 2006). We use the regularization

$$\boldsymbol{D}\left(\boldsymbol{a}^{(2)}\right) = \begin{cases} \xi e^{\frac{\ln(10)T}{10}}(1 - 3a_{ij}^{(2)})||\boldsymbol{C}||_2 & \text{if } i = j \\ \xi e^{\frac{\ln(10)T}{10}}(-3a_{ij}^{(2)})||\boldsymbol{C}||_2 & \text{if } i \neq j \end{cases}, \tag{27}$$

with $\xi = 2.0 \times 10^{-3}$.

The temperature was determined using the standard advection-diffusion equation,

$$\rho_{\mathrm{i}} q \left(\frac{\partial T}{\partial t} + \boldsymbol{u} \cdot \nabla T\right) = \nabla \cdot (\kappa \nabla T) + \Psi, \tag{28}$$

where q and κ are the heat capacity and conductivity of ice, respectively, and $\Psi = \boldsymbol{\sigma} : \dot{\boldsymbol{\epsilon}}$ is the strain heating.

Horizontal shear is large in much of the NEGIS catchment, and occurs out of the plane of the 2.5-D model used here. $\dot{\epsilon}_{\tilde{x}\tilde{y}}$ is therefore parameterized in the fabric evolution equations. The portion of horizontal shear experienced in the model plane is

$$\dot{\epsilon}_{\tilde{x}\tilde{y}} = \frac{1}{2}\frac{\partial u}{\partial \tilde{y}} - \frac{u}{2r}, \tag{29}$$

where r is the radius of curvature of the flowline. We assume that the intensity of shear at depth scales with the along-flow velocity so

$$\frac{\partial u}{\partial \tilde{y}} \approx \frac{\partial u_{\mathrm{s}}}{\partial \tilde{y}} \frac{u(z)}{u_{\mathrm{s}}} \tag{30}$$

where u_{s} is the surface velocity. Combining (29) and (30), the horizontal shear strain rate in model coordinates can be approximated as

$$\dot{\epsilon}_{\tilde{x}\tilde{y}}(z) \simeq \frac{1}{2}\left(\frac{\partial u_{\mathrm{s}}}{\partial \tilde{y}} \frac{u(z)}{u_{\mathrm{s}}} - \frac{u(z)}{r}\right). \tag{31}$$

We neglect the contribution of $\dot{\epsilon}_{\tilde{x}z}$ to the fabric evolution, since that term can be shown to be small (Reeh, 1988). In addition, we neglect the effect of the horizontal shear upon the effective viscosity but include it in the temperature evolution. Before each simulation, we calculated r and $\frac{\partial u_s}{\partial \tilde{y}}$ for each model domain from a multi-year InSAR composite (Joughin et al., 2018), smoothed to 2-km resolution, and these remained fixed throughout the model runs.

3.1.2 Simulations

We ran the model along a set of 31 flowlines in the upper catchment of NEGIS. At closest approach to the EGRIP core site, model domains were separated by 2.5 km across flow (leading to a total width of 75 km spanned by the domains). Each model domain is 2.5D, i.e. a flowband, following a flowline while accounting for transverse convergence/divergence. We found W by tracing particle paths upstream in the measured InSAR velocities (Joughin et al., 2018), starting from a flowband half-width of 2.5 times the ice thickness (total flowband width ∼12.5 km) near the EGRIP core site. Flowbands are wide enough to average out some of the effects of small-scale topography that can detrimentally affect flowline models (Sergienko, 2012), but overlap with each other at some points (Fig. 10). Note that convergence towards the ice stream leads to significant narrowing of the central flowbands, while outer bands experience little effect from the extra half dimension. The ice surface and bed elevations defining the model geometry were determined using the average values in the across-flow directions from ArcticDEM (Porter et al., 2018) and Bedmachine v3 (Morlighem et al., 2017), respectively. In order to perform all calculations in ice-equivalent thickness, surface elevations were modified by subtracting 18 m everywhere to account for the firn-air content as estimated from RACMO 2.3.1 (Ligtenberg et al., 2018). Each model domain used a triangular mesh with 100-m vertical and 250-m horizontal resolution. For each flowband, we ran a 5-kyr transient

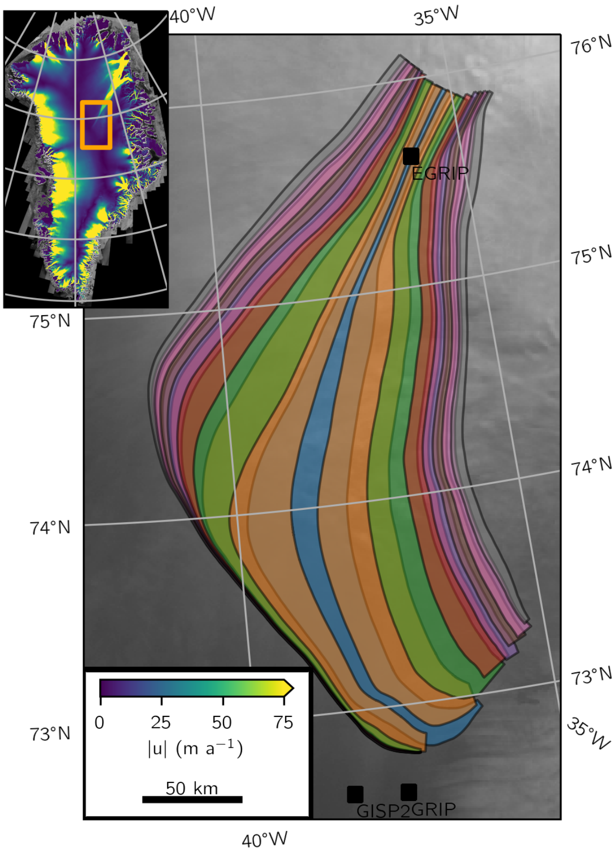

Figure 10: Model domains of the Elmer/Ice flow model. Every other domain across flow is plotted. Background from RADARSAT (Joughin et al., 2016). Inset shows location in Greenland, plotted atop ice-flow velocities (Joughin et al., 2018).

simulation, after which changes in fabric in the areas of interest were negligible. Initial conditions were reasonable guesses for fabric and temperature, but simulations were long enough that there is no sensitivity to the exact choice. Time stepping used a second-order backwards difference with variable time steps of 0.01–1.0 years.

3.1.3 Boundary Conditions

At the surface, we simply impose zero normal stress. The accumulation rate is taken to match the 1970–2016 mean from RACMO2.3 (Noël et al., 2015). At the basal boundary, we use the pattern of basal melt inferred from radar and 1-D modelling from MacGregor et al. (2016), with freeze-on zeroed out. In addition, we scale the overall pattern of basal mass loss in order to achieve mass balance (requiring a reduction of up to 50% compared to the published values), so that final ice thicknesses remained realistic.

At the downstream end of the domain, within the ice stream, we impose that the horizontal velocity matches the surface velocity at all depths, i.e. we force all motion to take place via sliding. Because we expected significant sensitivity to this assumption within a few ice thicknesses of the boundary, the model domains were designed to extend sufficiently far so as to isolate these effects from the area of interest. When motion is purely the result of sliding, Eq. (20) implies that vertical strain rate is constant, so the vertical velocity varies linearly with depth. We assume that the downstream boundary is at its steady state thickness, so impose that the vertical velocity varies linearly from the accumulation rate, i.e. $u_3(S) = -a$, at the surface to the melt rate at the bed.

At the inflow boundary, we impose a depth-variable horizontal velocity scaled to match observations at the surface (Joughin et al., 2018). Assuming that ice is isothermal, isotropic, and flows purely by internal deformation, the velocity can be shown to follow Raymond (1983)

$$u_{\text{in}}(z) = u_{\text{s,in}} \left[1 - \left(\frac{H_{\text{in}} - z}{H_{\text{in}}} \right)^{n+1} \right], \tag{32}$$

where H_{in} is the ice thickness at inflow, and we take $n = 4$ as an ad-hoc fit to the weakening from fabric and temperature found at depth within the model domain at $n = 3$.

To reasonably match observed surface velocities, the model requires a variable basal velocity. We imposed a spatially variable basal drag using the results of inverse modelling using a 3-dimensional model of the upper catchment of NEGIS, determined in the same manner as Holschuh et al. (2019) but updated to suit the region of interest here. We used a linear Weertman sliding law, i.e. $\tau_b = Bu^m$, where $m = 1$ and B was determined from the inverse results. In the final 2 km of the domain, the inversion-determined B was linearly tapered to zero to ensure a smooth transition to the plug-flow boundary condition we used there.

We assume that the surface ice is isotropic, while at the upstream end we impose the profile from the NorthGRIP ice core (Wang et al., 2002b), though the results are insensitive to this choice since memory of this condition is erased before the area of interest. For temperature boundary conditions, the surface is held at the 1970–2013 2-m temperature from RACMO 2.3 (Noël et al., 2015) and the geothermal heat flux at the base is taken from a global gridded product (Davies, 2013).

3.1.4 Results

Before analyzing results, we define the coordinate system to have flow at angle β counter clockwise from North Polar Stereographic east, and the largest fabric eigenvalue at θ^{geo} (Fig. 1). Note that for the fabric, angles are equivalent mod(180°), since c-axes do not have a direction, but we choose to define them to be in the range $0^\circ \leq \theta^{\text{geo}} \leq 180^\circ$. The depth-averaged horizontal eigenvalue differences are shown in Fig. 11. The range of $\Delta\lambda$ is 0–0.9, with 95% of values in the range 0–0.67. The very high values ($\Delta\lambda > 0.6$) imply a horizontal single maximum, intermediate values ($\Delta\lambda \sim$0.3-0.6) generally indicate a vertical girdle, and low values provide little information (vertical single maxima, weak vertical girdles, and isotropy all have weak horizontal anisotropy). At every point in map view, the depth-averaged $\Delta\lambda$ hides vertical structure; fabrics are universally isotropic in the surface, and are generally vertical single maxima near the bed, though in some regions the basal fabric is partway between a vertical girdle and vertical single maximum.

Horizontal shear causes rotation of the horizontal eigenvectors away from the model's $\tilde{x}$ and $\tilde{y}$ vectors (Fig. 11c), and generally leads to a horizontal single maximum near the ice-stream shear margins. The single maximum is stronger in the northwest margin than the southeast one, despite the northern margin being more diffuse. However, since the fabric results from the integrated strain history, this difference is unsurprising; due to residence times in the margin, the total horizontal shear experienced by a flowline is larger in the northwest margin. In geographic coordinates, the direction of the largest eigenvector is highly variable, as it is influenced both by shear and the flow direction, but it retains a notable transition at the shear margins (Fig. 11b).

3.1.5 Limitations

Though this is arguably the most advanced coupled model of fabric and flow, it still has a number of shortcomings, particularly for dynamic areas. First, the fabric evolution considers only lattice rotation; a number of studies suggest a role for dynamic recrystallization in the evolution fabric in warm ice, and even in colder ice when stress is high (see Faria et al., 2014, and references therein). While the full stress state is included the parameterized half dimension, the model is not fully three dimensional. As a result, the across-flow resolution is very coarse (effectively 2.5 km), and the horizontal shear stresses must be imposed. Imposing the horizontal stress requires smoothing of remotely sensed velocity products to obtain reasonable strain rates, which may degrade sharp gradients in the fabric. While the model assumes isotropic ice at the surface, ice cores often show anisotropic fabrics near the surface (Stoll et al., 2021; Westhoff et al., 2021). Despite these limitations,

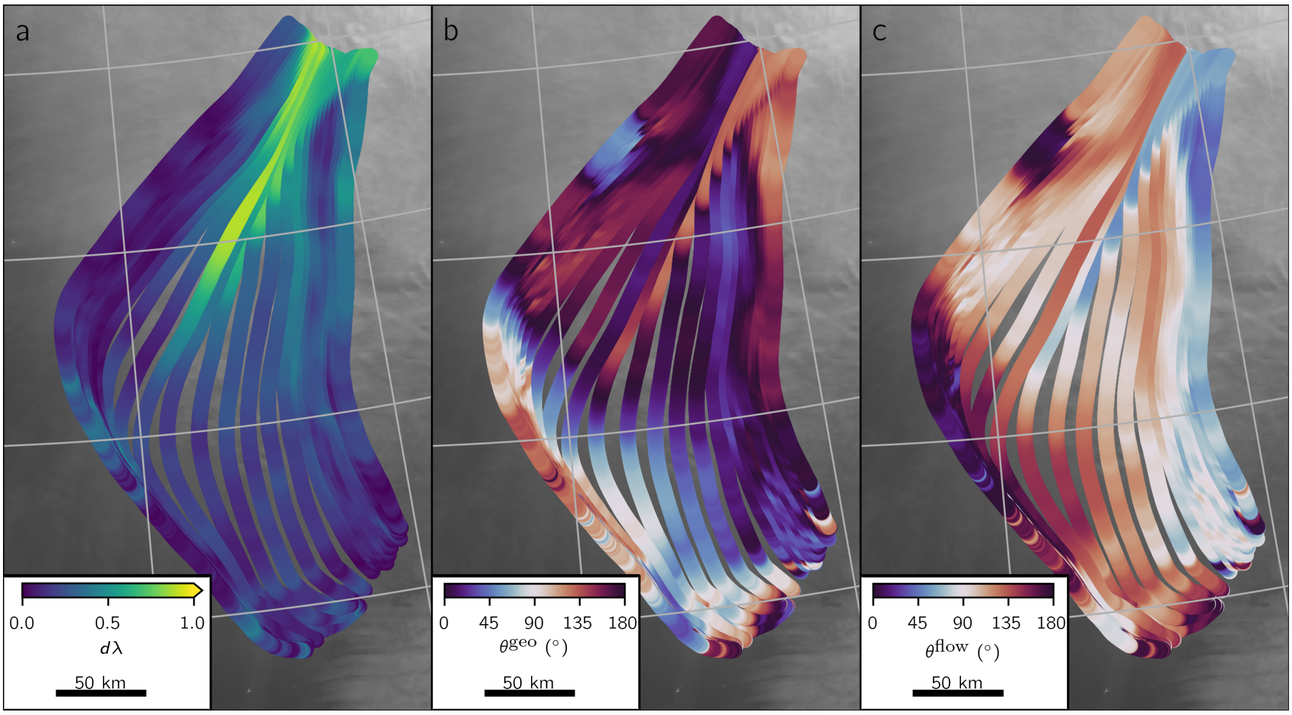

Figure 11: Results from anisotropic flow modelling. **a** The horizontal eigenvalue difference, $\Delta\lambda$. **b** The rotation of the largest horizontal eigenvector from Polar Stereographic x'. **c** The rotation of the largest horizontal eigenvector from model x.

the model matches the pattern of fabric inferred from radar and measured by ice cores well enough to provide a reasonable estimate of the fabric between data points.

3.2 Downstream fabric evolution modelling with 'Specfab'

Radar-inferred horizontal anisotropies over NEGIS decrease downstream of EGRIP. The model domain of our Elmer/Ice flow model simulations extends, however, only approximately 40 km downstream of EGRIP due to loss of numerical stability associated with higher down-stream ice flow velocities. Hence, the fabric evolution downstream cannot be validated with the ice flow model. Instead, we use the spectral fabric model for polycrystalline materials by Rathmann et al. (2021) to simulate the fabric evolution of an ice parcel along the flow line passing through EGRIP. The model is a kinematic model in the sense that c-axes rotate in response the velocity gradient field (apparent strain-induced rotation of c-axes), and not stress or temperature.

Specifically, we consider an ice parcel seeded at EGRIP with a girdle-type fabric that matches the average fabric measured in the ice-core (Westhoff et al., 2021),

$$\boldsymbol{a}^{(2)} = \begin{pmatrix} 0 & 0 & 0 \\ 0 & 0.6 & 0 \\ 0 & 0 & 0.4 \end{pmatrix}, \tag{33}$$

and let it travel downstream along a flow line derived by the MeASUREs multi-year surface velocity field (Joughin et al., 2018). The flow line is divided into segments of distance travelled in one year. For each segment, the strain-rate tensor, $\dot{\boldsymbol{\epsilon}}$, is derived from surface velocities in a curvelinear coordinate system following the flow line under an assumption of negligible vertical shear and incompressibility:

$$\dot{\epsilon}_{\tilde{x}\tilde{x}} = \frac{\partial u}{\partial \tilde{x}}, \quad \dot{\epsilon}_{\tilde{y}\tilde{y}} = \frac{\partial v}{\partial \tilde{y}}, \quad \dot{\epsilon}_{\tilde{z}\tilde{z}} = -\dot{\epsilon}_{\tilde{x}\tilde{x}} - \dot{\epsilon}_{\tilde{y}\tilde{y}}, \tag{34}$$

$$\dot{\epsilon}_{\tilde{x}\tilde{y}} = \frac{1}{2}\left(\frac{\partial u}{\partial \tilde{y}} + \frac{\partial v}{\partial \tilde{x}}\right) \quad \dot{\epsilon}_{\tilde{x}z} = \dot{\epsilon}_{\tilde{y}z} = 0. \tag{35}$$

In addition, the spin is assumed to vanish, as the flow line is relatively straight:

$$\frac{1}{2}\left(\tilde{\nabla}\mathbf{u} - (\tilde{\nabla}\mathbf{u})^{\mathrm{T}}\right) = \mathbf{0}. \tag{36}$$

For each one-year time-step, the Lagrangian update to the parcel's fabric is given by the strain-rate and spin tensors over the traversed flow-line segment. The end of the flow-line corresponds to 2000 years downstream of EGRIP. Figure 12 shows snapshots of the corresponding normalized c-axes distribution (orientation distribution function) at intervals of 1000 years. The initial girdle is found to slowly evolve into near-isotropic ice at the downstream end of the flowline. We emphasize, however, that the fabric evolution model is a linear partial differential equation. As such, any unaccounted, superimposed mode of deformation would lead to a corresponding superimposed imprint on the modelled c-axis distributions. For example, if vertical simple shear is present (not modelled here), a superimposed vertical single-maximum is to be expected that has little-to-no horizontal anisotropy. Such contributions to the total fabric pattern are, however, not detectable by our radar methodology which requires horizontal anisotropy to be present.

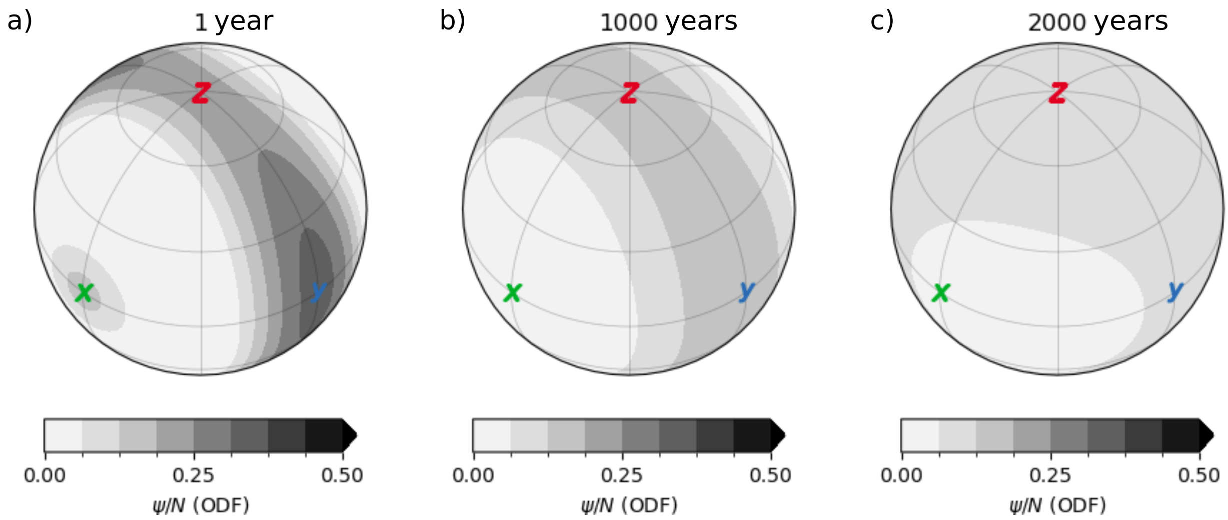

Figure 12: Fabric evolution along a downstream flowline starting at EGRIP. The EGRIP-type girdle in **a)** transforms rapidly into a weaker girdle shown in **b)** before it dissolves almost entirely into near-isotropic ice in **c)**. The fabric was calculated using the 'specfab' model developed by Rathmann et al. (2021), with strain-rate tensors derived from the surface velocities (Joughin et al., 2018).

4 Flow enhancement factors

To evaluate the effect that the inferred crystal fabric has upon ice flow, we calculate the bulk directional enhancement factors following Rathmann et al. (2021) and Rathmann and Lilien (2021), defined as the anisotropic-to-isotropic strain-rate ratio (Thorsteinsson, 2001)

$$E_{vw} = \frac{\dot{\epsilon}_{vw}}{\dot{\epsilon}_{vw}^{\mathrm{iso}}}, \tag{37}$$

where vw indicates the component (direction) of interest, and $\dot{\epsilon}_{vw}$ is the corresponding component of the bulk strain-rate tensor. While the denominator in Eq. (37) can be replaced by Glen's isotropic flow law, the numerator requires an anisotropic rheology that depends on the fabric state. The latter can be estimated by averaging a transversely isotropic monocrystal rheology over all grain orientations, with monocrystal rheological parameters chosen such that observed, bulk directional enhancements are reproduced (Rathmann et al., 2021; Rathmann and Lilien, 2021). For this purpose, a linear-viscous monocrystal rheology has previously been suggested to suffice upon carefully selecting a polycrystal stress–strain-rate homogenization scheme (Rathmann and Lilien, 2021). We refer the reader to Rathmann and Lilien (2021) for details, but find it instructive to write out the bulk strain rate resulting from assuming a pure stress homogenization:

$$\dot{\boldsymbol{\epsilon}} = \langle \dot{\boldsymbol{\epsilon}}'(\boldsymbol{\tau}) \rangle = A' \left[\boldsymbol{\tau} - \frac{E'_{cc} - 1}{2} (\boldsymbol{\tau} \cdot\cdot \langle \boldsymbol{c}^2 \rangle) \boldsymbol{I} + \frac{3(E'_{cc} - 1) - 4(E'_{ca} - 1)}{2} \boldsymbol{\tau} \cdot\cdot \langle \boldsymbol{c}^4 \rangle \right.$$
$$\left. + (E'_{ca} - 1)(\boldsymbol{\tau} \cdot \langle \boldsymbol{c}^2 \rangle + \langle \boldsymbol{c}^2 \rangle \cdot \boldsymbol{\tau}) \right], \quad (38)$$

where $\boldsymbol{\tau}$ is the bulk deviatoric stress tensor, E'_{cc} and E'_{ca} are the monocrystal strain-rate enhancements for compression and extension along the c-axis and shearing along the basal plane, respectively, $\boldsymbol{I}$ is the identity, and A' is an isotropic rate factor. From this simple model (38), it is clear that the bulk enhancements effectively depend on the second and fourth-order structure tensors, $\langle \boldsymbol{c}^2 \rangle$ and $\langle \boldsymbol{c}^4 \rangle$, defined as the average over the second and fourth outer product of the individual crystal orientations ($\boldsymbol{c}_i$):

$$\boldsymbol{a}^{(2)} = \langle \boldsymbol{c}^2 \rangle = \frac{1}{N} \sum_i^N \boldsymbol{c}_i \otimes \boldsymbol{c}_i, \quad (39)$$

and

$$\boldsymbol{a}^{(4)} = \langle \boldsymbol{c}^4 \rangle = \frac{1}{N} \sum_i^N \boldsymbol{c}_i \otimes \boldsymbol{c}_i \otimes \boldsymbol{c}_i \otimes \boldsymbol{c}_i. \quad (40)$$

In the more complicated mixed stress–strain-rate homogenization scheme used here, the resulting enhancements also depend on the fabric as quantified by $\boldsymbol{a}^{(2)}$ and $\boldsymbol{a}^{(4)}$ (not shown).

Notice that due to division in Eq. (37), the enhancement factors are independent of A' and the magnitude of the stress tensor. The same applies, in principle, to other isotropic contributions to the viscosity, such as temperature and impurities, insofar so they can be captured by modifying A'.

Finally, we note that in the case of a single-maximum or girdle fabric, the principal fabric directions can be taken without ambiguity to be the eigenvectors of $\boldsymbol{a}^{(2)}$. If one eigenvector is aligned with the vertical z-direction, $\boldsymbol{a}^{(2)}$ can be written in its eigenbasis as

$$\boldsymbol{a}^{(2)} = \begin{pmatrix} \lambda_x & 0 & 0 \\ 0 & \lambda_y & 0 \\ 0 & 0 & \lambda_z \end{pmatrix}. \quad (41)$$

4.1 Estimating the second-order structure tensor from horizontal anisotropy

Our observatioal methodologies allow for inferring the difference in horizontal eigenvalues only, $\Delta\lambda = \lambda_y - \lambda_x$. However, by applying a few assumptions about the fabric type to be expected over the different regions of NEGIS, guided by ice-core fabric observations from EGRIP and its shear margin, $\boldsymbol{a}^{(2)}$ can be reconstructed from $\Delta\lambda$:

1. **Inside the ice stream**: both the fabric evolution model and the EGRIP ice core indicate the presence of a girdle in the ice stream centre, so that $\lambda_x \approx 0$. If combined with the definitions $\lambda_x + \lambda_y + \lambda_z = 1$ and $\Delta\lambda = \lambda_y - \lambda_x$, it follows that:

$$\begin{aligned} \lambda_x &= 0, \\ \lambda_y &= \Delta\lambda, \\ \lambda_z &= 1 - \Delta\lambda, \end{aligned} \quad (42)$$

   or equivalently

$$\mathbf{a}^{(2)} = \begin{pmatrix} 0 & 0 & 0 \\ 0 & \Delta\lambda & 0 \\ 0 & 0 & 1 - \Delta\lambda \end{pmatrix}. \quad (43)$$

2. **In the vicinity of the shear margins:** Ice cores and our fabric evolution modelling indicate the formation of strong horizontal single-maximum fabrics in the shear margin and its vicinity, with the largest-eigenvalue eigenvector pointing approximately perpendicular to the shear margin. We thus propose that $\lambda_x \approx \lambda_z$, from which it follows that

$$\begin{aligned} \lambda_x \approx \lambda_z \approx \tfrac{1-\Delta\lambda}{3}, \\ \lambda_y \approx \tfrac{1+2\Delta\lambda}{3}, \end{aligned} \tag{44}$$

and therefore

$$\mathbf{a}^{(2)} = \begin{pmatrix} \frac{1-\Delta\lambda}{3} & 0 & 0 \\ 0 & \frac{1+2\Delta\lambda}{3} & 0 \\ 0 & 0 & \frac{1-\Delta\lambda}{3} \end{pmatrix}. \tag{45}$$

3. **Outside the shear margins:** In this regime, we lack direct observations from ice cores. Modelling results suggest that λ_x is small, but not zero. We therefore assume the more relaxed condition $\lambda_x \approx 0.1$, from which it follows that

$$\begin{aligned} \lambda_x &= 0.1, \\ \lambda_y &= 0.1 + \Delta\lambda, \\ \lambda_z &= 0.8 - \Delta\lambda, \end{aligned} \tag{46}$$

and therefore

$$\mathbf{a}^{(2)} = \begin{pmatrix} 0.1 & 0 & 0 \\ 0 & 0.1+\Delta\lambda & 0 \\ 0 & 0 & 0.8-\Delta\lambda \end{pmatrix}. \tag{47}$$

4.2 Estimating the fourth-order structure tensor from the second-order tensor

In order to estimate the directional enhancement factors, both $\boldsymbol{a}^{(2)}$ and $\boldsymbol{a}^{(4)}$ must be known. Although our methodology is restricted in providing only $\boldsymbol{a}^{(2)}$ from radar observations, $\boldsymbol{a}^{(4)}$ can be calculated from correlations with $\boldsymbol{a}^{(2)}$, derived from ice-core fabrics and fabric modelling, as elaborated on in the following.

The structure tensors, Eqs. (39) and (40), can be calculated from the second- ($l = 2$) and fourth-order ($l = 4$) complex expansion coefficients of the orientation distribution function (ODF) (Rathmann et al., 2021)

$$\mathrm{ODF}(\vartheta, \varphi) = \frac{1}{N} \sum_{l=0}^{\infty} \sum_{m=-l}^{l} \psi_l^m Y_l^m(\vartheta, \varphi), \tag{48}$$

where Y_l^m are the spherical harmonic expansion functions, depending on the co-latitude ϑ and longitude φ, and ψ_l^m are the complex expansion coefficients. In the case of a perfect single-maximum or girdle fabric (as considered here), the independent expansion coefficient reduce to just two real numbers. This follows immediately from the fact that if the fabric is rotated into a frame where it is horizontally symmetric, only ψ_2^0 and ψ_4^0 can be nonzero (only the modes Y_l^0 are rotationally symmetric around the z axis). As a consequence, if a correlation can be constructed between ψ_2^0 and ψ_4^0, then $\boldsymbol{a}^{(4)}$ can be constructed from $\boldsymbol{a}^{(2)}$ for single maximum and girdle fabrics since $\boldsymbol{a}^{(2)}$ depends exclusively on ψ_2^m (Rathmann et al., 2021).

Figure 13 shows a scatter plot of measured correlations (markers) between ψ_2^0 and ψ_4^0, calculated from published c-axis data from ice cores drilled at domes and extentional/flank flows sites (references provided in the figure text). Note that all c-axes distributions have been rotated into a frame where they are approximately rotationally symmetric around the z-axis for this method to work; of course, once the correlation has been applied to determine ψ_4^0, the resulting ODF can be rotated back into its original orientation.

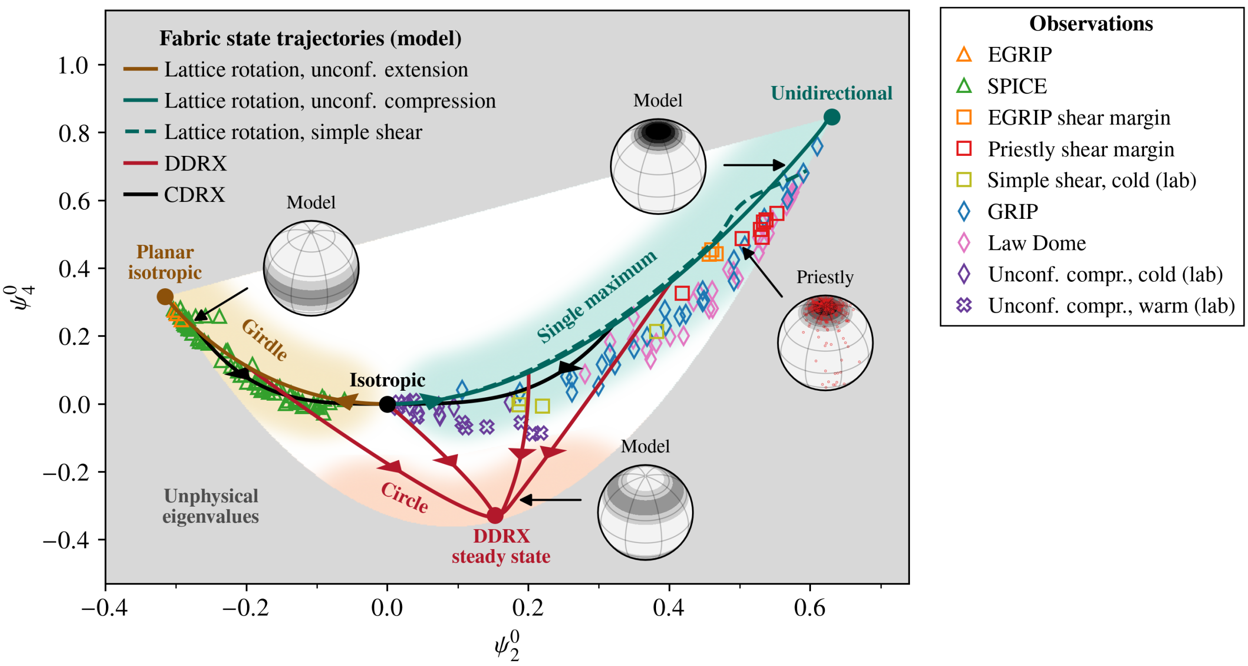

Figure 13: Correlation between the forth-order spectral coefficient, ψ_4^0, and the second-order coefficient, ψ_2^0, for fabrics with a horizontal isotropy. Ice-core girdle fabrics from EGRIP (Westhoff et al., 2021) and SPICE (Voigt et al., 2017) follow the model-predicted correlation for unconfined extension (full brown line). For single maximum fabrics, ice-core data (Thomas et al., 2021; Thorsteinsson et al., 1997b; Treverrow et al., 2016) and deformation tests (Fan et al., 2020; Qi et al., 2019) tend to fall slightly below the modeled correlation line predicted for unconfined compression (full green line) and simple shear (dashed green line), possibly due to the influence of discontinuous dynamic recrystallization (DDRX) or rotation recrystallization (CDRX) (modelled effects indicated by red and black paths, respectively; see main text). Both cores taken in our survey area (red markers), however, agree well with the modelled correlation. Grey regions indicate nonphysical eigenvalues for horizontally isotropic ODFs.

The full lines in Fig. 13 show the corresponding modelled effect of lattice rotation (strain-induced rotation of c-axes) using the model by Rathmann et al. (2021), shown here for unconfined extension, leading to a perfect girdle, and for unconfined compression, leading to a perfect single maximum. Although the observed correlation for single-maximum fabrics falls slight below the model line, fabric samples from the EGRIP ice core (red squares) agree well with the modelled correlation, as does the NEGIS shear margin ice core (red triangles). In this work, we therefore assume that the correlation between ψ_2^0 and ψ_4^0 is given exactly by the modelled correlation (full line). We find, however, that the effect of discontinuous migration recrystallization (DDRX; dotted light grey line) and continuous recrystallization (CDRX; dashed dark grey line) might explain the discrepancy between observed and modelled correlations elsewhere.

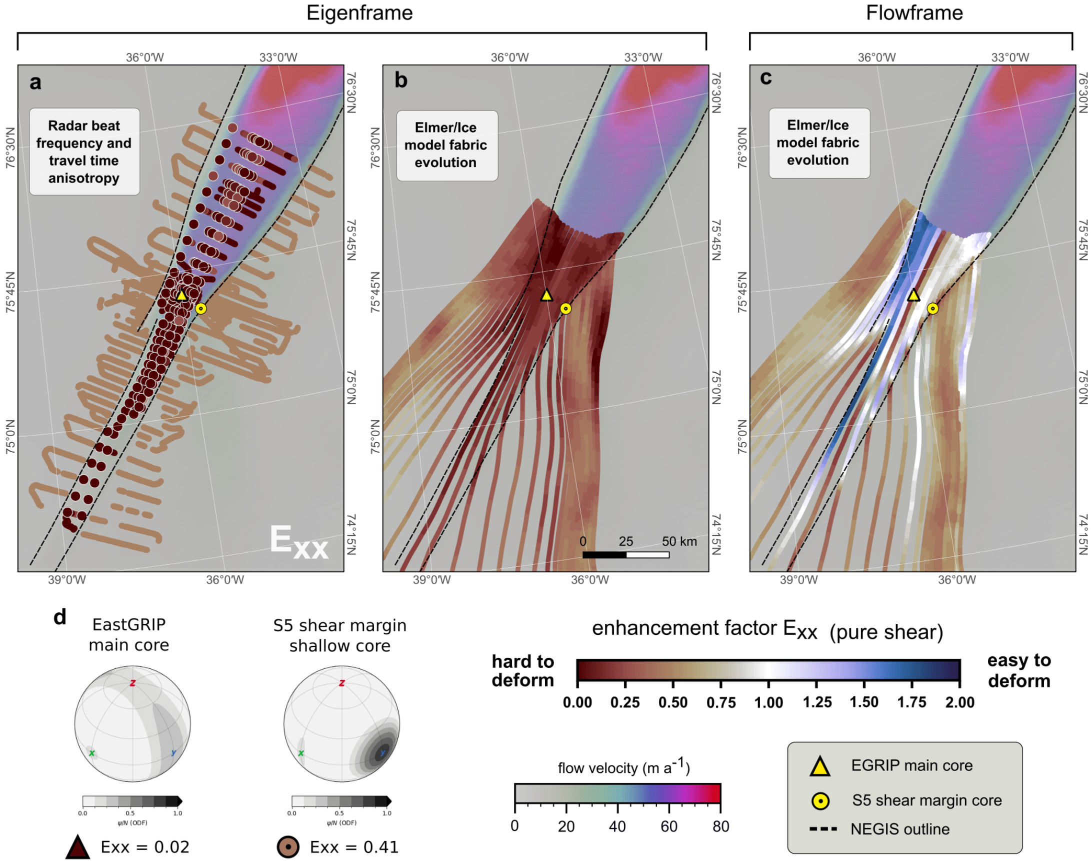

Figure 14: Enhancement factor E_{xx} (pure shear along ice flow). Panel (a) shows the enhancement factors derived from the radar measurements (both from the crosspoint analysis and beat frequency anisotropy analysis). Panel (b) and (c) show the enhancement factors derived from the Elmer/Ice fabric modeling. Note that Panels (a) and (b) represent the enhancement factors with respect to the *eigenframe* and panel (c) with respect to the *flowframe*. The respective stereographic projections of the c-axes and enhancement factors derived from the two ice-core locations (EastGRIP main core and S5 shear margin core) are shown in (d).

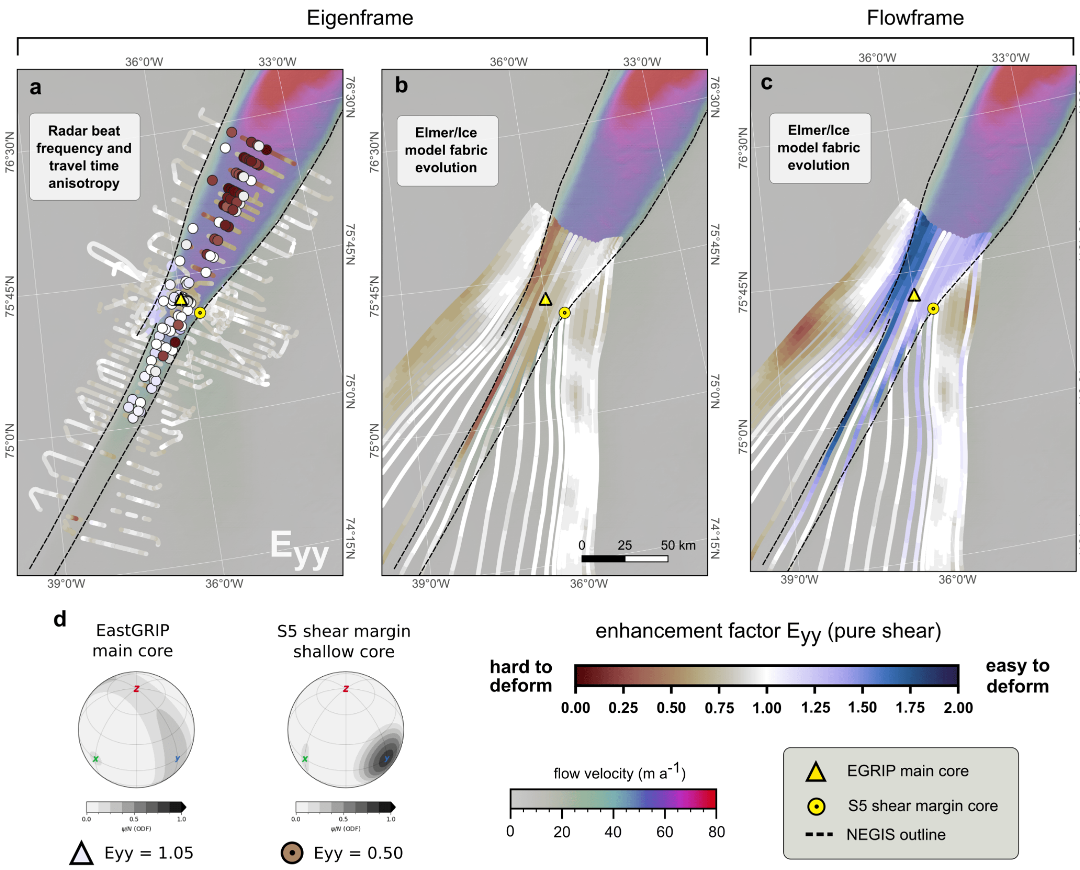

Figure 15: Enhancement factor E_{yy} (pure shear perpendicular to ice flow). Panel (a) shows the enhancement factors derived from the radar measurements (both from the crosspoint analysis and beat frequency anisotropy analysis). Panel (b) and (c) show the enhancement factors derived from the Elmer/Ice fabric modeling. Note that Panels (a) and (b) represent the enhancement factors with respect to the *eigenframe* and panel (c) with respect to the *flowframe*. The respective stereographic projections of the c-axes and enhancement factors derived from the two ice-core locations (EastGRIP main core and S5 shear margin core) are shown in (d).

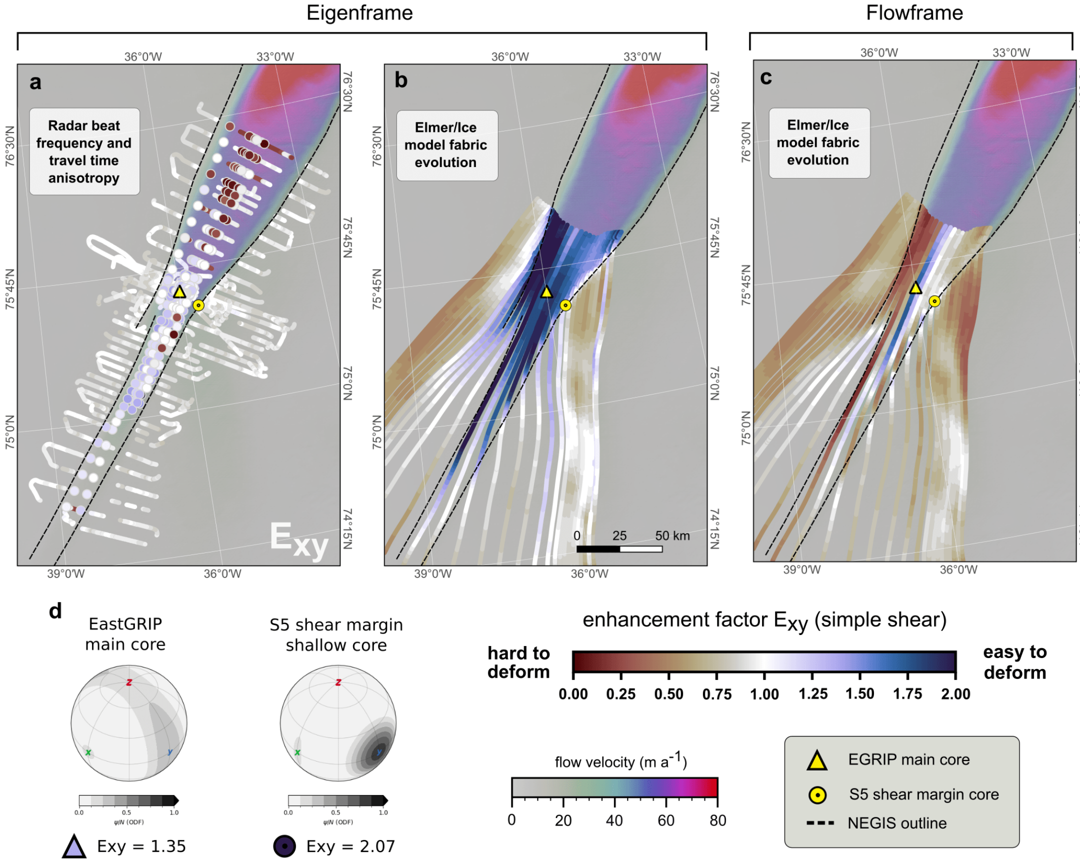

Figure 16: Enhancement factor E_{xy} (simple shear along to ice flow). Panel (a) shows the enhancement factors derived from the radar measurements (both from the crosspoint analysis and beat frequency anisotropy analysis). Panel (b) and (c) show the enhancement factors derived from the Elmer/Ice fabric modeling. Note that Panels (a) and (b) represent the enhancement factors with respect to the *eigenframe* and panel (c) with respect to the *flowframe*. The respective stereographic projections of the c-axes and enhancement factors derived from the two ice-core locations (EastGRIP main core and S5 shear margin core) are shown in (d).

5 Equivalent enhancement due to temperature

Temperature is, besides the fabric effects, the most important factor controlling the ice viscosity. To evaluate the potential significance of either effect, we estimate the equivalent temperature difference required to obtain a similar enhancement in the corresponding direction from the enhancement factors provided above. Modified to the effect of temperature, Eq. (37) becomes:

$$E = \frac{\dot{\epsilon}(\boldsymbol{\tau}, T_2)}{\dot{\epsilon}(\boldsymbol{\tau}, T_1)} = \frac{A(T_2)\boldsymbol{\tau}^n}{A(T_1)\boldsymbol{\tau}^n}. \tag{49}$$

At temperatures below –10°C, the temperature dependence of the creep parameter A can be described by a simple Arrhenius relationship

$$E = \frac{A_0 \exp(-\frac{Q}{RT_2})\boldsymbol{\tau}^n}{A_0 \exp(-\frac{Q}{RT_1})\boldsymbol{\tau}^n} = \exp\left(\frac{Q}{R}\left(\frac{1}{T_1} - \frac{1}{T_2}\right)\right), \tag{50}$$

whereby the prefactor A_0 and the stress tensor $\boldsymbol{\tau}^n$ cancel out and R is the universal gas constant. Field measurements and laboratory measurements show that the activation energy Q is approximately 60 kJmol^{-1} for temperatures below –10°C (Weertman, 1983).

The temperatures T_1, T_2 are given in Kelvin, and can be expressed as $\Delta T = T_2 - T_1$. Equation (50) can thus be re-written as

$$\Delta T = \frac{{T_1}^2 \frac{R}{Q} \ln(E)}{1 - T_1 \frac{R}{Q} \ln(E)}. \tag{51}$$

Here, we assume that the reference temperature T_1 equals –20°C. We find that the resulting temperature anomaly relevant for the obtained enhancements is relatively insensitive toward the choice of T_1, as long as the ice is colder than –10°C (Fig. 17). For higher temperatures, however, the assumed value of the activation energy Q no longer holds, implying that similar enhancements could be achieved by smaller temperature anomalies in the presence of temperate ice. While this could possibly be relevant in the shear margins, we believe that temperate ice is unlikely to be found in major parts of the ice column inside and outside the ice stream. Fig. 18–20 show the temperature anomalies (ΔT) which would be required to obtain similar viscosities as for the directional enhancements due to fabric (Fig. 14–16).

6 Characteristic time

The characteristic time for a viscous response is defined as

$$\tau_{char} = \frac{(2 + 2\mu)\eta}{E}, \tag{52}$$

where the Poisson ratio μ in ice can be assumed to be 0.325, and the Young's modulus E is approximately 10^9 Pa. An enhancement of 0.1, equivalent to the viscosity η being ten times larger than for isotropic ice, would imply that the characteristic time is ten times smaller. Ergo, a viscous deformation happens ten times faster in ice that is harder for pure-shear deformation along-flow in comparison to isotropy.

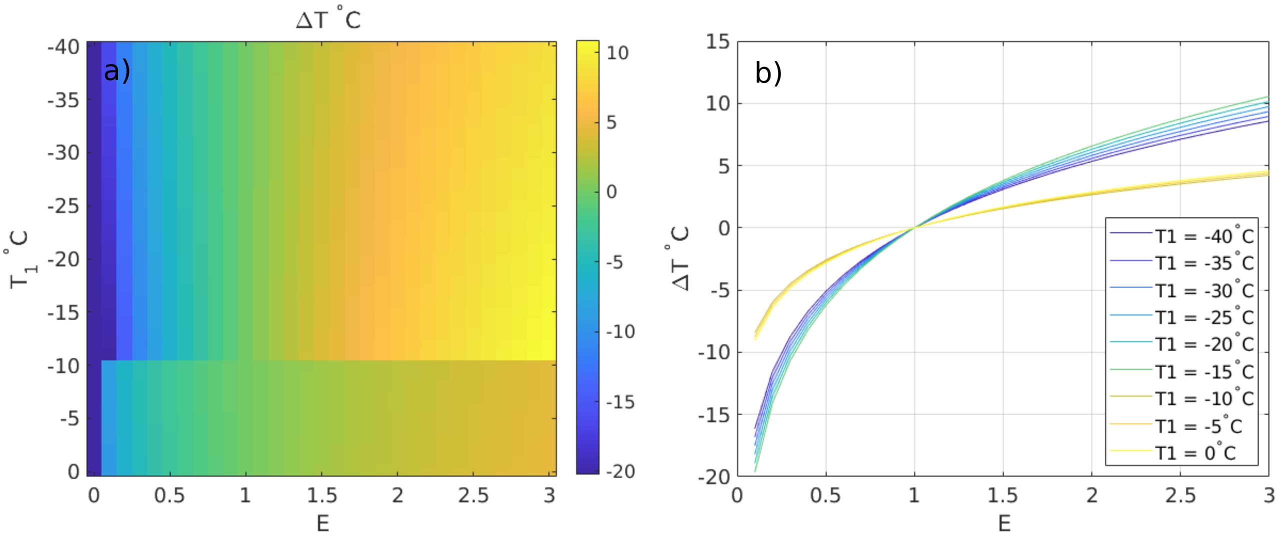

Figure 17: **a)** Temperature difference ΔT for varying enhancement factors E and a given reference temperature T_1. **b)** Sensitivity of ΔT on the choice of the reference temperature T_1. For temperatures below –20°C the activation energy Q is assumed to be 60 kJmol^{-1} whereas for temperatures above –10°C Q=152 kJmol^{-1} is assumed, leading to a stronger effect on the flow enhancement for smaller temperature variations than for colder ice. Within the two temperature regimes the sensitivity to T_1 is minor.

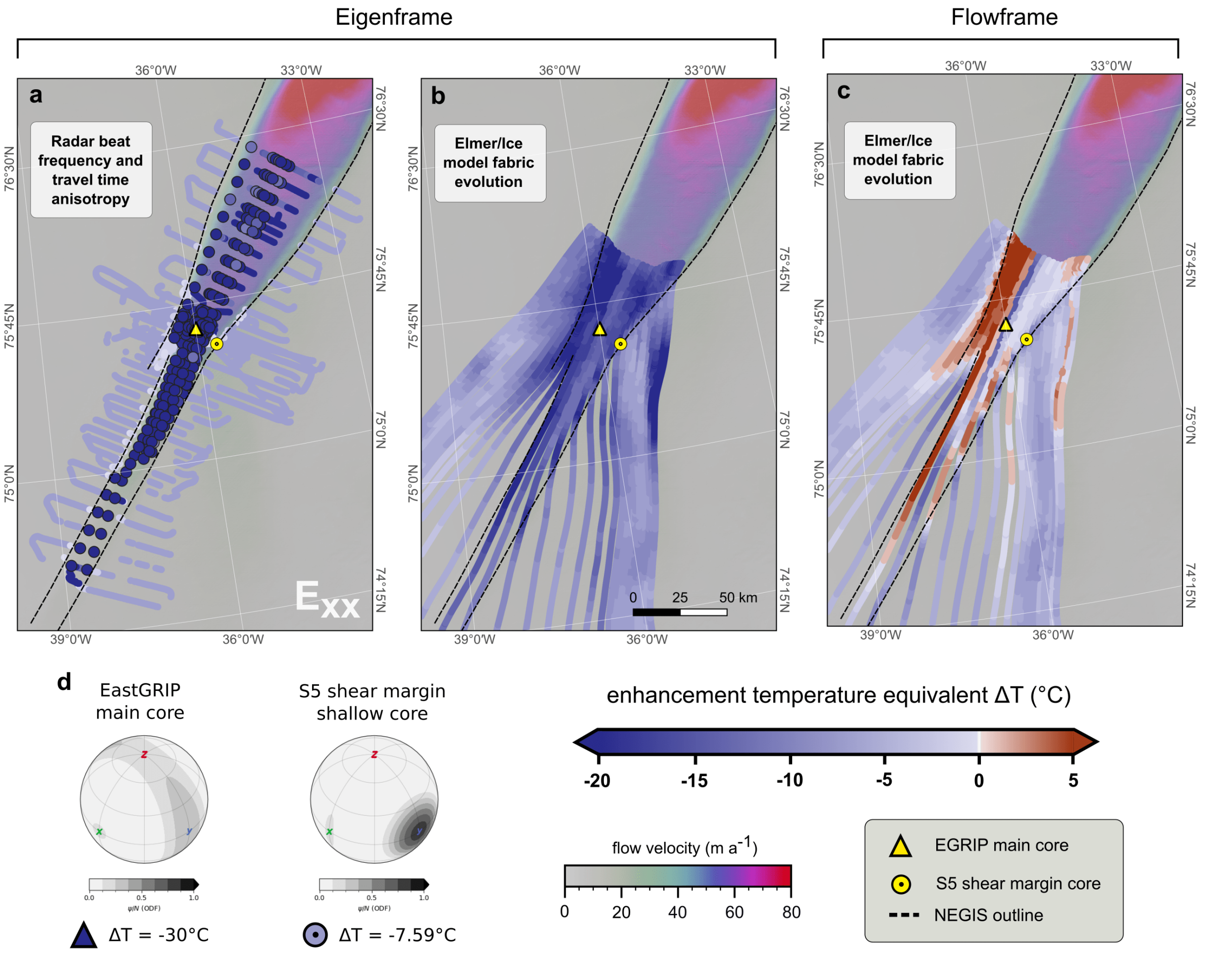

Figure 18: Temperature anomaly ΔT which would be required to obtain an (isotropic) flow enhancement as suggested by the fabric for pure-shear deformation along flow (E_{xx}). Akin to Fig. 14, panel **a)** shows the temperature anomalies equivalent to the enhancements obtained from radar observations, **b)** and **c)** those for the modeling results in eigenframe and flowframe respectively, and **d)** correspond to the observations in the two ice cores. Temperature anomalies are calculated for a reference temperature of –20°C.

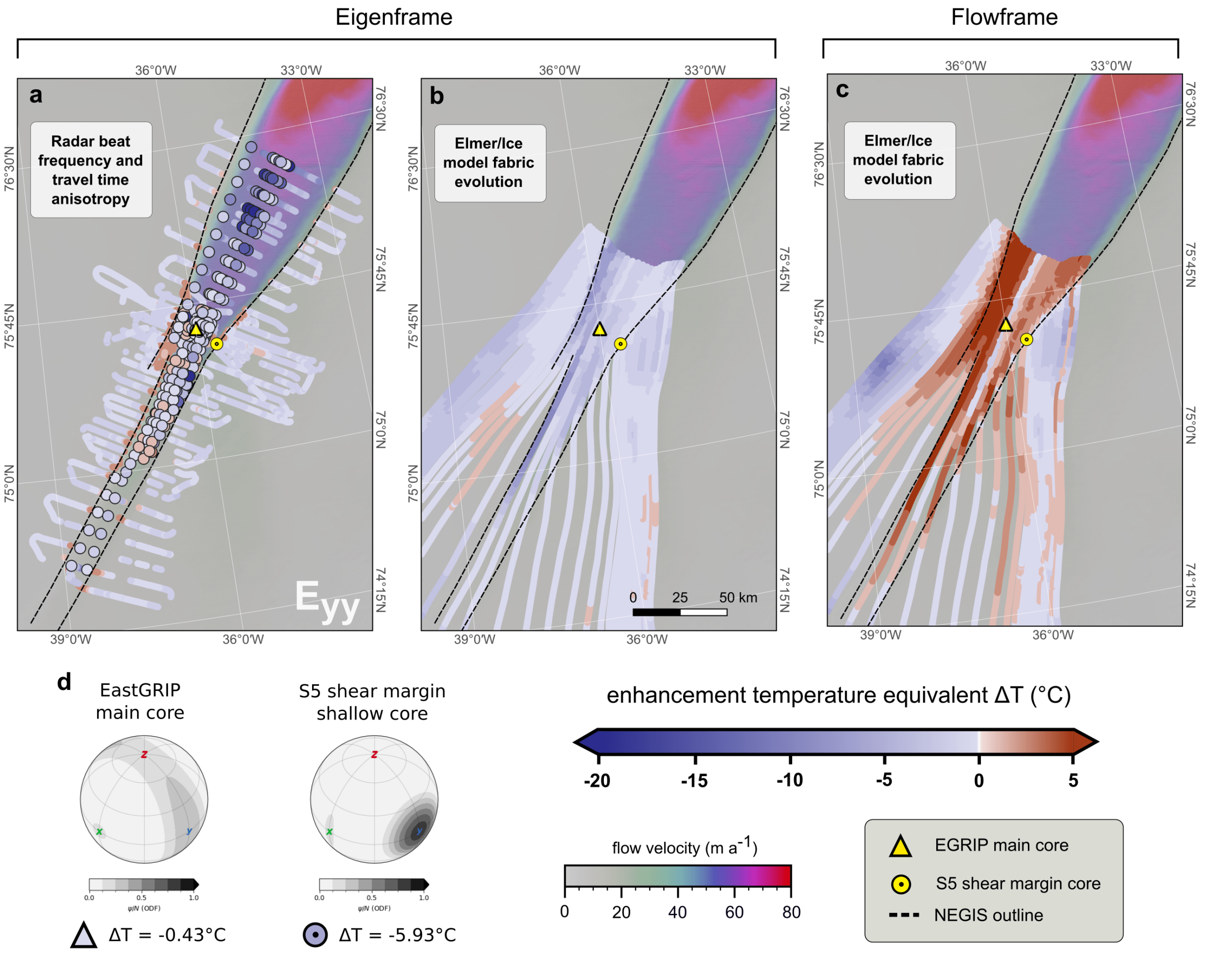

Figure 19: Temperature anomaly ΔT which would be required to obtain an (isotropic) flow enhancement as suggested by the fabric for pure-shear deformation perpendicular to flow (E_{yy}). Akin to Fig. 15, panel **a)** shows the temperature anomalies equivalent to the enhancements obtained from radar observations, **b)** and **c)** those for the modeling results in eigenframe and flowframe respectively, and **d)** correspond to the observations in the two ice cores. Temperature anomalies are calculated for a reference temperature of –20°C.

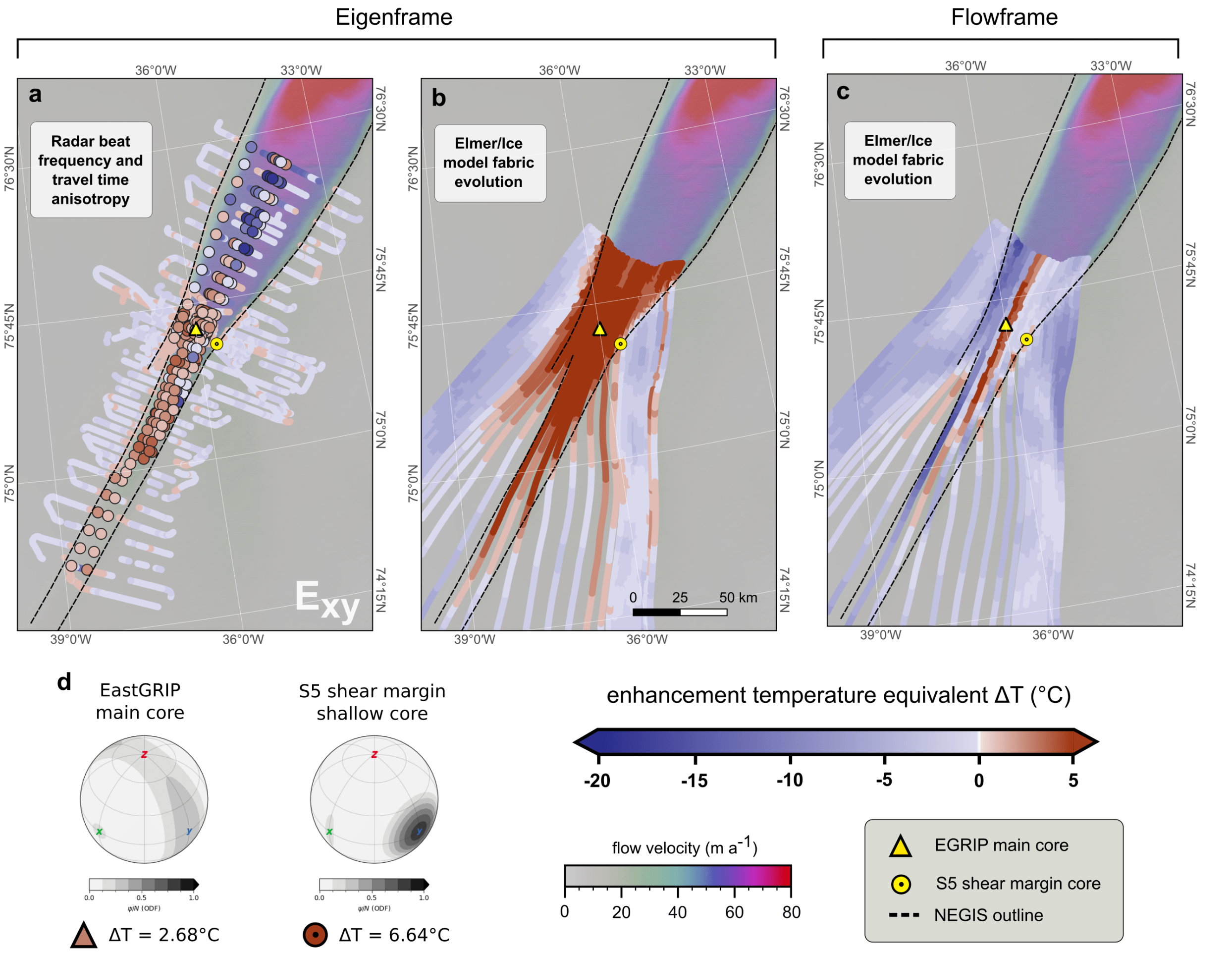

Figure 20: Temperature anomaly ΔT which would be required to obtain an (isotropic) flow enhancement as suggested by the fabric for horizontal simple-shear deformation (E_{xy}). Akin to Fig. 16, panel **a)** shows the temperature anomalies equivalent to the enhancements obtained from radar observations, **b)** and **c)** those for the modeling results in eigenframe and flowframe respectively, and **d)** correspond to the observations in the two ice cores. Temperature anomalies are calculated for a reference temperature of –20°C.

7 Notation (not exhaustive)

x', y'	geographic east, north
$\tilde{x}, \tilde{y}$	direction parallel, transverse to ice flow
$\hat{x}, \hat{y}$	flow-parallel, flow perpendicular radar antenna polarization
x, y	direction of smaller, larger horizontal eigenvalue
z	depth below ice sheet surface
θ^{flow}	angle between ice flow direction and largest horizontal fabric eigenvector
θ^{geo}	angle between geographic east and largest horizontal fabric eigenvector
θ^{pol}	angle between radar polarizatiosn and horizontal fabric eigenvectors
β	angle between geographic east and ice flow direction
$\boldsymbol{a}^{(2)}$, $\boldsymbol{a}^{(4)}$	second, fourth order fabric orientation tensor
$\boldsymbol{a}_{1,2,3}$	fabric eigenvectors
$\lambda_{1,2,3}$, $\lambda_{x,y,z}$	fabric eigenvalues of increasing size, in x, y, z direction
$\varepsilon*$	complex dielectric constant
ε, ε_0	relative dielectric permittivity, permittivity of free space
γ	electrical conductivity
κ	thermal conductivity
ω	angular frequency
$\boldsymbol{\varepsilon}^m, \boldsymbol{\varepsilon}$	dielectric permittivity tensor for monocrystal, polycristal
$\varepsilon^m_{\parallel}, \varepsilon^m_{\perp}$	dielectric permittivity parallel, perpendicular to the c-axis
$\Delta\varepsilon^m$, $\Delta\varepsilon$	dielectric anisotropy of a monocrystal, polycrystal
ε_{xy}	horizontal mean of relative dielectric permittivity of a polycrystal
$\Delta\varepsilon_a$	apparent horizontal dielectric anisotropy between radar polarization directions $\tilde{x}$ and $\tilde{y}$
$\Delta\lambda_a$	apparent difference in horizontal eigenvalues between radar polarization directions
$\Delta\lambda$	difference in horizontal eigenvalues
c, c_0	electromagnetic wave speed, speed of light
E_x, E_y	electromagnetic wave components in principal fabric directions x and y
$t_{\hat{x}}, t_{\hat{y}}$	two-way travel time for $\hat{x}$, $\hat{y}$ polarized wave reflection
$\bar{t}$,Δt	mean, difference of two-way travel time between waves with different antenna polarization
$\overline{\varepsilon_{\hat{x}}}$,$\overline{\varepsilon_{\hat{y}}}$	depth-averaged directional permittivities
ϕ	phase difference between ordinary and extraordinary wave
f	centre frequency of radar system
f_{mod},T_{mod}	power modulation frequency, period
k	wave number

$\boldsymbol{u}, \boldsymbol{v}, \boldsymbol{w}$ ice flow velocities flow-parallel, flow-transverse, vertical

$\boldsymbol{\sigma}$ Cauchy stress tensor

ρ_i density of ice

g force of gravity

$\boldsymbol{\tau}$ deviatoric stress tensor

$\boldsymbol{M}_{1,2,3}$ structure tensors

n flow law exponent

A flow-law prefactor

T temperature

$W(\tilde{x})$ width of flowband

$\boldsymbol{W}$ spin tensor

$\dot{\boldsymbol{\epsilon}}$ strain rate tensor

Ψ strain heating

r flowline curvature

H ice thickness

η ice viscosity

q heat capacity

E_{vw} flow enhancement factor in direction vw

E'_{cc}, E'_{ca} enhancement of a monocrystal along the c-axis, basal plane

$\boldsymbol{c}_i$ c-axis orientation of monocrystal

ψ_l^m complex spectral expansion coefficient

Y_l^m spherical harmonics expansion function

R universal gas constant

Q activation energy

References

Alley, R. B. (1988). "Fabrics in polar ice sheets: development and prediction". In: *Science* 240.4851, pp. 493–495. doi: 10.1126/science.240.4851.493.

Azuma, N. and Higashi, A. (1985). "Formation processes of ice fabric pattern in ice sheets". In: *Annals of Glaciology* 6, pp. 130–134. doi: 10.3189/1985AoG6-1-130-134.

Azuma, N., Wang, Y., Mori, K., Narita, H., Hondoh, T., Shoji, H., and Watanabe, O. (1999). "Textures and fabrics in the Dome F (Antarctica) ice core". In: *Annals of Glaciology* 29, pp. 163–168. doi: 10.3189/172756499781821148.

Bouchez, J. and Duval, P. (1982). "The fabric of polycrystalline ice deformed in simple shear: experiments in torsion, natural deformation and geometrical interpretation". In: *Texture, Stress, and Microstructure* 5.3, pp. 171–190.

Castelnau, O., Shoji, H., Mangeney, A., Milsch, H., Duval, P., Miyamoto, A., Kawada, K., and Watanabe, O. (1998). "Anisotropic behavior of GRIP ices and flow in Central Greenland". In: *Earth and Planetary Science Letters* 154.1-4, pp. 307–322. doi: 10.1016/S0012-821X(97)00193-3.

Christianson, K., Peters, L. E., Alley, R. B., Anandakrishnan, S., Jacobel, R. W., Riverman, K. L., Muto, A., and Keisling, B. A. (2014). "Dilatant till facilitates ice-stream flow in northeast Greenland". In: *Earth and Planetary Science Letters* 401, pp. 57–69. doi: 10.1016/j.epsl.2014.05.060.

Cuffey, K., Conway, H., Gades, A. M., Hallet, B., Lorrain, R., Severinghaus, J. P., Steig, E. J., Vaughn, B., and White, J. W. (2000). "Entrainment at cold glacier beds". In: *Geology* 28.4, pp. 351–354. doi: 10.1130/0091-7613(2000)28<351:EACGB>2.0.CO;2.

Davies, J. H. (2013). "Global map of solid Earth surface heat flow". In: *Geochemistry, Geophysics, Geosystems* 14.10, pp. 4608–4622. doi: 10.1002/ggge.20271.

Diprinzio, C., Wilen, L., Alley, R., Fitzpatrick, J., Spencer, M., and Gow, A. (2005). "Fabric and texture at Siple Dome, Antarctica". In: *Journal of Glaciology* 51.173, pp. 281–290. doi: 10.3189/172756505781829359.

Durand, G., Gagliardini, O., Thorsteinsson, T., Svensson, A., Kipfstuhl, S., and Dahl-Jensen, D. (2006). "Ice microstructure and fabric: an up-to-date approach for measuring textures". In: *Journal of Glaciology* 52.179, pp. 619–630. doi: 10.3189/172756506781828377.

Durand, G., Svensson, A., Persson, A., Gagliardini, O., Gillet-Chaulet, F., Sjolte, J., Montagnat, M., and Dahl-Jensen, D. (2009). "Evolution of the texture along the EPICA Dome C ice core". In: *Low Temperature Science* 68.Supplement, pp. 91–105.

Duval, P., Ashby, M., and Anderman, I. (1983). "Rate-controlling processes in the creep of polycrystalline ice". In: *The Journal of Physical Chemistry* 87.21, pp. 4066–4074. doi: 10.1021/j100244a014.

Eisen, O., Hamann, I., Kipfstuhl, S., Steinhage, D., and Wilhelms, F. (2007). "Direct evidence for continuous radar reflector originating from changes in crystal-orientation fabric". In: *The Cryosphere* 1.1, pp. 1–10. doi: 10.5194/tc-1-1-2007.

Ershadi, M. R., Drews, R., Martın, C., Eisen, O., Ritz, C., Corr, H., Christmann, J., Zeising, O., Humbert, A., and Mulvaney, R. (2022). "Polarimetric radar reveals the spatial distribution of ice fabric at domes and divides in East Antarctica". In: *The Cryosphere* 16.5, pp. 1719–1739. doi: 10.5194/tc-16-1719-2022. url: https://tc.copernicus.org/articles/16/1719/2022/.

Fan, S., Hager, T. F., Prior, D. J., Cross, A. J., Goldsby, D. L., Qi, C., Negrini, M., and Wheeler, J. (2020). "Temperature and strain controls on ice deformation mechanisms: insights from the microstructures of samples deformed to progressively higher strains at -10, -20 and -30°C". In: *The Cryosphere* 14.11, pp. 3875–3905. doi: 10.5194/tc-14-3875-2020. url: https://tc.copernicus.org/articles/14/3875/2020/.

Faria, S. H., Weikusat, I., and Azuma, N. (2014). "The microstructure of polar ice. Part I: Highlights from ice core research". In: *Journal of Structural Geology* 61, pp. 2–20. doi: 10.1016/j.jsg.2013.09.010.

Fitzpatrick, J. J., Voigt, D. E., Fegyveresi, J. M., Stevens, N. T., Spencer, M. K., Cole-Dai, J., Alley, R. B., Jardine, G. E., Cravens, E. D., Wilen, L. A., et al. (2014). "Physical properties of the WAIS Divide ice core". In: *Journal of Glaciology* 60.224, pp. 1181–1198. doi: 10.3189/2014JoG14J100.

Franke, S., Jansen, D., Binder, T., Paden, J. D., Dörr, N., Gerber, T. A., Miller, H., Dahl-Jensen, D., Helm, V., Steinhage, D., et al. (2022). "Airborne ultra-wideband radar sounding over the shear margins and along flow lines at the onset region of the Northeast Greenland Ice Stream". In: *Earth System Science Data* 14.2, pp. 763–779. DOI: 10.5194/essd-14-763-2022.

Fujita, S., Maeno, H., and Matsuoka, K. (2006). "Radio-wave depolarization and scattering within ice sheets: a matrix-based model to link radar and ice-core measurements and its application". In: *Journal of Glaciology* 52.178, pp. 407–424. DOI: 10.3189/172756506781828548.

Gagliardini, O. and Meyssonnier, J. (1999). "Analytical derivations for the behavior and fabric evolution of a linear orthotropic ice polycrystal". In: *Journal of Geophysical Research: Solid Earth* 104.B8, pp. 17797–17809. DOI: 10.1029/1999JB900146.

Gardner, A., Fahnestock, M., and Scambos, T. (2021). *ITS_LIVE regional glacier and ice sheet surface velocities, Colorado: Data archived at National Snow and Ice Data Center.* DOI: 10.5067/6II6VW8LLWJ7.

Gerbi, C., Mills, S., Clavette, R., Campbell, S., Bernsen, S., Clemens-Sewall, D., Lee, I., Hawley, R., Kreutz, K., Hruby, K., and al., et (2021). "Microstructures in a shear margin: Jarvis Glacier, Alaska". In: *Journal of Glaciology* 67.266, pp. 1163–1176. DOI: 10.1017/jog.2021.62.

Gillet-Chaulet, F., Gagliardini, O., Meyssonnier, J., Montagnat, M., and Castelnau, O. (2005). "A user-friendly anisotropic flow law for ice-sheet modelling". In: *Journal of Glaciology* 51.172, pp. 3–14. DOI: 10.3189/172756505781829584.

Gillet-Chaulet, F., Gagliardini, O., Meyssonnier, J., Zwinger, T., and Ruokolainen, J. (2006). "Flow-induced anisotropy in polar ice and related ice-sheet flow modelling". In: *J. Non-Newtonian Fluid Mech* 134, pp. 33–43. DOI: 10.1016/j.jnnfm.2005.11.005.

Gow, A., Meese, D., Alley, R., Fitzpatrick, J., Anandakrishnan, S., Woods, G., and Elder, B. (1997). "Physical and structural properties of the Greenland Ice Sheet Project 2 ice core: A review". In: *Journal of Geophysical Research: Oceans* 102.C12, pp. 26559–26575. DOI: 10.1029/97JC00165.

Gow, A. J. and Williamson, T. (1976). "Rheological implications of the internal structure and crystal fabrics of the West Antarctic ice sheet as revealed by deep core drilling at Byrd Station". In: *Geological Society of America Bulletin* 87.12, pp. 1665–1677. DOI: 10.1130/0016-7606(1976)87<1665:RIOTIS>2.0.CO;2.

Herron, S. L. and Langway, C. C. (1982). "A comparison of ice fabrics and textures at Camp Century, Greenland and Byrd Station, Antarctica". In: *Annals of glaciology* 3, pp. 118–124. DOI: 10.3189/S0260305500002639.

Holschuh, N., Lilien, D. A., and Christianson, K. (2019). "Thermal Weakening, Convergent Flow, and Vertical Heat Transport in the Northeast Greenland Ice Stream Shear Margins". In: *Geophysical Research Letters* 46.14, pp. 8184–8193. DOI: 10.1029/2019GL083436.

Hvidberg, C. S. (1996). "Steady-state thermomechanical modelling of ice flow near the centre of large ice sheets with the finite-element technique". In: *Annals of Glaciology* 23, pp. 116–123. DOI: 10.3189/S026030550001332X.

Jordan, T. M., Schroeder, D. M., Castelletti, D., Li, J., and Dall, J. (2019). "A polarimetric coherence method to determine ice crystal orientation fabric from radar sounding: application to the NEEM Ice Core Region". In: *IEEE Transactions on Geoscience and Remote Sensing* 57.11, pp. 8641–8657. DOI: 10.1109/TGRS.2019.2921980.

Joughin, I., Smith, B. E., and Howat, I. M. (2018). "A complete map of Greenland ice velocity derived from satellite data collected over 20 years". In: *Journal of Glaciology* 64.243, pp. 1–11. DOI: 10.1017/jog.2017.73.

Joughin, I. R., Smith, B. E., Howat, I. M., Moon, T., and Scambos, T. A. (2016). "A SAR record of early 21st century change in Greenland". In: *Journal of Glaciology* 62.231, pp. 1–10. DOI: 10.1017/jog.2016.10.

Journaux, B., Chauve, T., Montagnat, M., Tommasi, A., Barou, F., Mainprice, D., and Gest, L. (2019). "Recrystallization processes, microstructure and crystallographic preferred orientation evolution in polycrystalline ice during high-temperature simple shear". In: *The Cryosphere* 13.5, pp. 1495–1511. DOI: 10.5194/tc-13-1495-2019.

Kamb, B. (1972). "Experimental recrystallization of ice under stress". In: *Washington DC American Geophysical Union Geophysical Monograph Series* 16, pp. 211–241. DOI: 10.1029/GM016p0211.

Kamb, W. B. (1959). “Ice petrofabric observations from Blue Glacier, Washington, in relation to theory and experiment”. In: *Journal of Geophysical Research* 64.11, pp. 1891–1909. DOI: 10.1086/626571.

Ligtenberg, S. R. M., Kuipers Munneke, P., Noël, B. P. Y., and Broeke, M. R. van den (2018). “Brief communication: Improved simulation of the present-day Greenland firn layer (1960–2016)”. In: *The Cryosphere* 12.5, pp. 1643–1649. DOI: 10.5194/tc-12-1643-2018.

Lipenkov, V. Y., Barkov, N., Duval, P., and Pimienta, P. (1989). “Crystalline texture of the 2083 m ice core at Vostok Station, Antarctica”. In: *Journal of Glaciology* 35.121, pp. 392–398. DOI: 10.3189/S0022143000009321.

Ma, Y., Gagliardini, O., Ritz, C., Gillet-Chaulet, F., Durand, G., and Montagnat, M. (2010). “Enhancement factors for grounded ice and ice shelves inferred from an anisotropic ice-flow model”. In: *Journal of Glaciology* 56.199, pp. 805–812. DOI: 10.3189/002214310794457209.

MacGregor, J. A., Fahnestock, M. A., Catania, G. A., Aschwanden, A., Clow, G. D., Colgan, W. T., Gogineni, S. P., Morlighem, M., Nowicki, S. M. J., Paden, J. D., Price, S. F., and Seroussi, H. (2016). “A synthesis of the basal thermal state of the Greenland Ice Sheet”. In: *Journal of Geophysical Research: Earth Surface* 121.7, pp. 1328–1350. DOI: 10.1002/2015JF003803.

Matsuoka, K., Power, D., Fujita, S., and Raymond, C. F. (2012). “Rapid development of anisotropic ice-crystal-alignment fabrics inferred from englacial radar polarimetry, central West Antarctica”. In: *Journal of Geophysical Research: Earth Surface* 117.F3. DOI: 10.1029/2012JF002440.

Matsuoka, T., Fujita, S., Morishima, S., and Mae, S. (1997). “Precise measurement of dielectric anisotropy in ice Ih at 39 GHz”. In: *Journal of Applied Physics* 81.5, pp. 2344–2348. DOI: 10.1063/1.364238.

Mojtabavi, S., Eisen, O., Franke, S., Jansen, D., Steinhage, D., Paden, J., Dahl-Jensen, D., Weikusat, I., Eichler, J., and Wilhelms, F. (2022). “Origin of englacial stratigraphy at three deep ice core sites of the Greenland Ice Sheet by synthetic radar modelling”. In: *Journal of Glaciology*, pp. 1–13. DOI: 10.1017/jog.2021.137.

Mojtabavi, S., Wilhelms, F., Cook, E., Davies, S. M., Sinnl, G., Skov Jensen, M., Dahl-Jensen, D., Svensson, A., Vinther, B. M., Kipfstuhl, S., et al. (2020). “A first chronology for the East Greenland Ice-core Project (EGRIP) over the Holocene and last glacial termination”. In: *Climate of the Past* 16.6, pp. 2359–2380. DOI: 10.5194/cp-16-2359-2020.

Montagnat, M., Azuma, N., Dahl-Jensen, D., Eichler, J., Fujita, S., Gillet-Chaulet, F., Kipfstuhl, S., Samyn, D., Svensson, A., and Weikusat, I. (2014). “Fabric along the NEEM ice core, Greenland, and its comparison with GRIP and NGRIP ice cores”. In: *The Cryosphere* 8.4, pp. 1129–1138. DOI: 10.5194/tc-8-1129-2014.

Montagnat, M., Buiron, D., Arnaud, L., Broquet, A., Schlitz, P., Jacob, R., and Kipfstuhl, S. (2012). “Measurements and numerical simulation of fabric evolution along the Talos Dome ice core, Antarctica”. In: *Earth and Planetary Science Letters* 357, pp. 168–178. DOI: 10.1016/j.epsl.2012.09.025.

Monz, M. E., Hudleston, P. J., Prior, D. J., Michels, Z., Fan, S., Negrini, M., Langhorne, P. J., and Qi, C. (2021). “Full crystallographic orientation (*c* and *a* axes) of warm, coarse-grained ice in a shear-dominated setting: a case study, Storglaciären, Sweden”. In: *The Cryosphere* 15.1, pp. 303–324. DOI: 10.5194/tc-15-303-2021.

Morlighem, M., Williams, C. N., Rignot, E., An, L., Arndt, J. E., Bamber, J. L., Catania, G., Chauché, N., Dowdeswell, J. A., Dorschel, B., Fenty, I., Hogan, K., Howat, I., Hubbard, A., Jakobsson, M., Jordan, T. M., Kjeldsen, K. K., Millan, R., Mayer, L., Mouginot, J., Noël, B. P. Y., O’Cofaigh, C., Palmer, S., Rysgaard, S., Seroussi, H., Siegert, M. J., Slabon, P., Straneo, F., Broeke, M. R. van den, Weinrebe, W., Wood, M., and Zinglersen, K. B. (2017). “BedMachine v3: Complete Bed Topography and Ocean Bathymetry Mapping of Greenland From Multibeam Echo Sounding Combined With Mass Conservation”. In: *Geophysical Research Letters* 44.21, pp. 11, 051–11, 061. DOI: 10.1002/2017GL074954.

Noël, B., Van De Berg, W. J., Van Meijgaard, E., Kuipers Munneke, P., Van De Wal, R. S. W., and Van Den Broeke, M. R. (2015). “Evaluation of the updated regional climate model RACMO2.3 :

Summer snowfall impact on the Greenland Ice Sheet". In: *The Cryosphere* 9.5, pp. 1831–1844. DOI: http://dx.doi.org/10.5194/tc-9-1831-2015.

Oraschewski, F. M. and Grinsted, A. (2021). "Modeling enhanced firn densification due to strain softening". In: *The Cryosphere Discussions*, pp. 1–24.

Paren, J. and Robin, G. d. Q. (1975). "Internal reflections in polar ice sheets". In: *Journal of Glaciology* 14.71, pp. 251–259. DOI: 10.3189/S0022143000021730.

Porter, C., Morin, P., Howat, I., Noh, M. J., Bates, B., Peterman, K., Keesey, S., Schlenk, M., Gardiner, J., and Tomko, K. (2018). "ArcticDEM". In: *Harvard Dataverse* 1.

Qi, C., Prior, D. J., Craw, L., Fan, S., Llorens, M.-G., Griera, A., Negrini, M., Bons, P. D., and Goldsby, D. L. (2019). "Crystallographic preferred orientations of ice deformed in direct-shear experiments at low temperatures". English. In: *The Cryosphere* 13.1, pp. 351–371. DOI: 10.5194/tc-13-351-2019.

Rathmann, N. M., Hvidberg, C. S., Grinsted, A., Lilien, D. A., and Dahl-Jensen, D. (2021). "Effect of an orientation-dependent non-linear grain fluidity on bulk directional enhancement factors". In: *Journal of Glaciology* 67.263, pp. 569–575. DOI: 10.1017/jog.2020.117.

Rathmann, N. M. and Lilien, D. A. (2021). "Inferred basal friction and mass flux affected by crystal-orientation fabrics". In: *Journal of Glaciology*, pp. 1–17. DOI: 10.1017/jog.2021.88.

Raymond, C. F. (1983). "Deformation in the Vicinity of Ice Divides". In: *Journal of Glaciology* 29.103, pp. 357–373. DOI: 10.3189/S0022143000030288.

Reeh, N. (1988). "A Flow-line Model for Calculating the Surface Profile and the Velocity, Strain-rate, and Stress Fields in an Ice Sheet". In: *Journal of Glaciology* 34.116, pp. 46–55. DOI: 10.3189/S0022143000009059.

Riverman, K. L., Alley, R. B., Anandakrishnan, S., Christianson, K., Holschuh, N. D., Medley, B., Muto, A., and Peters, L. E. (2019). "Enhanced Firn Densification in High-Accumulation Shear Margins of the NE Greenland Ice Stream". In: *Journal of Geophysical Research: Earth Surface* 124.2, pp. 365–382. DOI: 10.1029/2017JF004604.

Robin, G. d. Q., Evans, S., and Bailey, J. T. (1969). "Interpretation of radio echo sounding in polar ice sheets". In: *Philosophical Transactions of the Royal Society of London. Series A, Mathematical and Physical Sciences* 265.1166, pp. 437–505. DOI: 10.1098/rsta.1969.0063.

Samyn, D., Svensson, A., and Fitzsimons, S. (2008). "Dynamic implications of discontinuous recrystallization in cold basal ice: Taylor Glacier, Antarctica". In: *Journal of Geophysical Research: Earth Surface* 113.F3. DOI: 10.1029/2006JF000600.

Sergienko, O. V. (2012). "The effects of transverse bed topography variations in ice-flow models". In: *Journal of Geophysical Research: Earth Surface* 117.F3, n/a–n/a. DOI: 10.1029/2011JF002203.

Stewart, C. L., Christoffersen, P., Nicholls, K. W., Williams, M. J., and Dowdeswell, J. A. (2019). "Basal melting of Ross Ice Shelf from solar heat absorption in an ice-front polynya". In: *Nature Geoscience* 12.6, p. 435. DOI: 10.1038/s41561-019-0356-0.

Stewart, C. L. (2018). "Ice-ocean interactions beneath the north-western Ross Ice Shelf, Antarctica". PhD thesis. University of Cambridge. DOI: 10.17863/CAM.21483.

Stoll, N., Eichler, J., Hörhold, M., Erhardt, T., Jensen, C., and Weikusat, I. (2021). "Microstructure, micro-inclusions, and mineralogy along the EGRIP ice core–Part 1: Localisation of inclusions and deformation patterns". In: *The Cryosphere* 15.12, pp. 5717–5737. DOI: 10.5194/tc-15-5717-2021.

Thomas, R. E., Negrini, M., Prior, D. J., Mulvaney, R., Still, H., Bowman, M. H., Craw, L., Fan, S., Hubbard, B., Hulbe, C., et al. (2021). "Microstructure and crystallographic preferred orientations of an azimuthally oriented ice core from a lateral shear margin: Priestley Glacier, Antarctica". In: *Frontiers in Earth Science* 9. DOI: 10.3389/feart.2021.702213.

Thorsteinsson, T., Kipfstuhl, J., and Miller, H. (1997a). "Textures and fabrics in the GRIP ice core". In: *Journal of Geophysical Research: Oceans* 102.C12, pp. 26583–26599. DOI: 10.1029/97JC00161.

Thorsteinsson, T., Kipfstuhl, J., and Miller, H. (1997b). "Textures and fabrics in the GRIP ice core". In: *Journal of Geophysical Research: Oceans* 102.C12, pp. 26583–26599. DOI: https://doi.org/10.1029/97JC00161. URL: https://agupubs.onlinelibrary.wiley.com/doi/abs/10.1029/97JC00161.

Thorsteinsson, T. (2001). "An analytical approach to deformation of anisotropic ice-crystal aggregates". In: *Journal of Glaciology* 47.158, pp. 507–516. DOI: 10.3189/172756501781832124.

Treverrow, A., Jun, L., and Jacka, T. H. (2016). "Ice crystal *c*-axis orientation and mean grain size measurements from the Dome Summit South ice core, Law Dome, East Antarctica". In: *Earth System Science Data* 8.1, pp. 253–263. DOI: 10.5194/essd-8-253-2016. URL: https://essd.copernicus.org/articles/8/253/2016/.

Vallelonga, P., Christianson, K., Alley, R., Anandakrishnan, S., Christian, J., Dahl-Jensen, D., Gkinis, V., Holme, C., Jacobel, R., Karlsson, N., et al. (2014). "Initial results from geophysical surveys and shallow coring of the Northeast Greenland Ice Stream (NEGIS)". In: *The Cryosphere* 8.4, pp. 1275–1287. DOI: 10.5194/tc-8-1275-2014.

Vaňková, I., Nicholls, K. W., Corr, H. F., Makinson, K., and Brennan, P. V. (2020). "Observations of tidal melt and vertical strain at the Filchner-Ronne Ice Shelf, Antarctica". In: *Journal of Geophysical Research: Earth Surface* 125.1, e2019JF005280. DOI: 10.1029/2019JF005280.

Voigt, D. et al. (2017). "c-axis fabric of the South pole ice core". In: *SPC14. US Antarctic Program (USAP) Data Center. Dataset. doi* 10, p. 601057. DOI: 10.15784/601057.

Wang, Y., Thorsteinsson, T., Kipfstuhl, J., Miller, H., Dahl-Jensen, D., and Shoji, H. (2002a). "A vertical girdle fabric in the NorthGRIP deep ice core, North Greenland". In: *Annals of Glaciology* 35, pp. 515–520. DOI: 10.3189/172756402781817301.

Wang, Y., Thorsteinsson, T., Kipfstuhl, J., Miller, H., Dahl-Jensen, D., and Shoji, H. (2002b). "A vertical girdle fabric in the NorthGRIP deep ice core, North Greenland". In: *Annals of Glaciology* 35, pp. 515–520. DOI: 10.3189/172756402781817301.

Weertman, J. (1983). "CREEP DEFORMATION OF ICE". In: *Annual Review of Earth and Planetary Sciences* 11.1, pp. 215–240. DOI: 10.1146/annurev.ea.11.050183.001243. URL: https://doi.org/10.1146/annurev.ea.11.050183.001243.

Westhoff, J., Stoll, N., Franke, S., Weikusat, I., Bons, P., Kerch, J., Jansen, D., Kipfstuhl, S., and Dahl-Jensen, D. (2021). "A stratigraphy-based method for reconstructing ice core orientation". In: *Annals of Glaciology* 62.85-86, pp. 191–202. DOI: 10.1017/aog.2020.76.

Wilen, L., Diprinzio, C., Alley, R., and Azuma, N. (2003). "Development, principles, and applications of automated ice fabric analyzers". In: *Microscopy research and technique* 62.1, pp. 2–18. DOI: 10.1002/jemt.10380.

Wilhelms, F., Kipfstuhl, J., Miller, H., Heinloth, K., and Firestone, J. (1998). "Precise dielectric profiling of ice cores: a new device with improved guarding and its theory". In: *Journal of Glaciology* 44.146, pp. 171–174. DOI: 10.3189/S002214300000246X.

Wilson, C. J., Russell-Head, D. S., and Sim, H. M. (2003). "The application of an automated fabric analyzer system to the textural evolution of folded ice layers in shear zones". In: *Annals of Glaciology* 37, pp. 7–17. DOI: 10.3189/172756403781815401.

Woodcock, N. (1977). "Specification of fabric shapes using an eigenvalue method". In: *Geological Society of America Bulletin* 88.9, pp. 1231–1236. DOI: 10.1130/0016-7606(1977)88<1231:SOFSUA>2.0.CO;2.

Yan, J.-B., Li, L., Nunn, J. A., Dahl-Jensen, D., O'Neill, C., Taylor, R. A., Simpson, C. D., Wattal, S., Steinhage, D., Gogineni, P., et al. (2020). "Multiangle, frequency, and polarization radar measurement of ice sheets". In: *IEEE Journal of Selected Topics in Applied Earth Observations and Remote Sensing* 13, pp. 2070–2080. DOI: 10.1109/JSTARS.2020.2991682.

Young, T., Schroeder, D. M., Jordan, T. M., Christoffersen, P., Tulaczyk, S. M., Culberg, R., and Bienert, N. L. (2021). "Inferring ice fabric from birefringence loss in airborne radargrams: Application to the eastern shear margin of Thwaites Glacier, West Antarctica". In: *Journal of Geophysical Research: Earth Surface* 126.5, e2020JF006023. DOI: 10.1029/2020JF006023.

Zeising, O. and Humbert, A. (2021). "Indication of high basal melting at the EastGRIP drill site on the Northeast Greenland Ice Stream". In: *The Cryosphere* 15.7, pp. 3119–3128. DOI: 10.5194/tc-15-3119-2021.